



## RESEARCH ARTICLE

10.1029/2020JD032667

# Increasing Resolution and Resolving Convection Improve the Simulation of Cloud-Radiative Effects Over the North Atlantic

Fabian Senf<sup>1</sup> , Aiko Voigt<sup>2,3</sup> , Nicolas Clerbaux<sup>4</sup> , Anja Hünerbein<sup>1</sup> , and Hartwig Deneke<sup>1</sup>

<sup>1</sup>Leibniz Institute for Tropospheric Research, Leipzig, Germany, <sup>2</sup>Institute for Meteorology and Climate Research - Department Troposphere Research, Karlsruhe Institute of Technology, Karlsruhe, Germany, <sup>3</sup>Lamont-Doherty Earth Observatory, Columbia University, New York City, NY, USA, <sup>4</sup>Royal Meteorological Institute of Belgium, Brussels, Belgium

## Key Points:

- Biases in cloud-radiative effects become smaller as grid spacing is decreased, especially from 80 to 20 km
- Refinements down to 2.5 km substantially reduce shortwave CRE biases only when the convection scheme is disabled
- Compensating biases between longwave and shortwave become smaller for finer resolutions leading to more realistic radiation fluxes

## Supporting Information:

- Supporting Information S1

## Correspondence to:

F. Senf,  
senf@tropos.de

## Citation:

Senf, F., Voigt, A., Clerbaux, N., Hünerbein, A., & Deneke, M. (2020). Increasing resolution and resolving convection improves the simulation of cloud-radiative effects over the North Atlantic. *Journal of Geophysical Research: Atmospheres*, 125, e2020JD032667. <https://doi.org/10.1029/2020JD032667>

Received 24 FEB 2020

Accepted 31 AUG 2020

Accepted article online 9 SEP 2020

**Abstract** Clouds interact with atmospheric radiation and substantially modify the Earth's energy budget. Cloud formation processes occur over a vast range of spatial and temporal scales, which make their thorough numerical representation challenging. Therefore, the impact of parameter choices for simulations of cloud-radiative effects is assessed in the current study. Numerical experiments are carried out using the ICOSahedral Nonhydrostatic (ICON) model with varying grid spacings between 2.5 and 80 km and with different subgrid-scale parameterization approaches. Simulations are performed over the North Atlantic with either one-moment or two-moment microphysics and with convection being parameterized or explicitly resolved by grid-scale dynamics. Simulated cloud-radiative effects are compared to products derived from Meteosat measurements. Furthermore, a sophisticated cloud classification algorithm is applied to understand the differences and dependencies of simulated and observed cloud-radiative effects. The cloud classification algorithm developed for the satellite observations is also applied to the simulation output based on synthetic infrared brightness temperatures, a novel approach that is not impacted by changing insolation and guarantees a consistent and fair comparison. It is found that flux biases originate equally from clear-sky and cloudy parts of the radiation field. Simulated cloud amounts and cloud-radiative effects are dominated by marine, shallow clouds, and their behavior is highly resolution dependent. Bias compensation between shortwave and longwave flux biases, seen in the coarser simulations, is significantly diminished for higher resolutions. Based on the analysis results, it is argued that cloud-microphysical and cloud-radiative properties have to be adjusted to further improve agreement with observed cloud-radiative effects.

**Plain Language Summary** Clouds are a major challenge for climate science, and their effects are difficult to quantify. Clouds scatter sunlight back into space and thus prevent the Earth from warming up. But clouds also hold back heat radiation upwelling from the surface. Both effects typically compensate each other and thus lead to the net cloud-radiative effect. Computer programs that are used to simulate the climate—so-called climate models—often use very coarse grid-box sizes in their computational mesh. Cloud processes and their effects are represented in them in a very simplified way, which leads to problems. For this reason, this study deals with the question to what extent the simulations of cloud-radiative effects can be improved by choosing more precise descriptions of the cloud processes. To investigate this, different configurations of more realistic models were taken to simulate cloud formation over the North Atlantic. The resulting simulation data were compared to satellite observations. It could be shown that problematic biases of the coarser climate models are reduced if, as is usual in weather models, one switches to smaller grid-box sizes and improved descriptions of the cloud processes.

## 1. Introduction

Clouds are very effective in cooling the Earth. Clouds scatter sunlight back to space before it can be absorbed by the Earth's surface. They also trap longwave radiation originating from the warm surface and thus induce a counter-acting greenhouse effect (Ramanathan et al., 1989). In the global mean, the shortwave effect of clouds ( $-46$  to  $-48$   $\text{W m}^{-2}$ ) dominates over their longwave effect ( $26$ – $28$   $\text{W m}^{-2}$ ) in the

©2020. The Authors.

This is an open access article under the terms of the Creative Commons Attribution License, which permits use, distribution and reproduction in any medium, provided the original work is properly cited.

top-of-the-atmosphere (TOA) radiation budget, leading to a net negative cloud-radiative effect (CRE) of  $-18$  to  $-20 \text{ W m}^{-2}$  (Arking, 1991; Henderson et al., 2013; Stephens et al., 2012; Zelinka et al., 2017). The magnitude of net radiative effects becomes even larger and more important for cloud systems over the mid-latitude oceans, where the net CRE is more than twice the global average (see, e.g., Zelinka et al., 2017).

Cloud feedbacks, that is, the impact of changes in clouds on the TOA radiation budget, remain a major source of uncertainty in future climate projections (Boucher et al., 2013; Ceppi et al., 2017). Recent work indicates that the global-mean cloud feedback to global warming is likely positive, that is, cloud changes will lead to an additional warming (Ceppi et al., 2017). This is largely attributed to a reduction in low-level cloud amount and a rise of high-level clouds (Zelinka et al., 2017). Yet, significant uncertainties remain in the parameterization of clouds and their radiative effects, in particular regarding the treatment of cloud microphysical processes in climate models (Gettelman & Sherwood, 2016). Understanding clouds and their radiative changes is also relevant for regional climate change, as the simulated response of the atmospheric circulation to global warming is strongly shaped by clouds (Ceppi & Shepherd, 2017; Voigt & Shaw, 2015; Voigt et al., 2019).

The steady increase in computational power and advent of a new generation of models that can harness this power has begun to allow for global atmospheric simulations with horizontal grid spacings on the order of a few kilometers (e.g., Satoh et al., 2018; Stevens et al., 2019). In these high-resolution simulations, clouds and the atmospheric flow interact much more naturally than in current low-resolution models typically run with horizontal grid spacings of around 50 km. The explicit simulation of at least part of the cloud-scale circulations in fact provides a physical link between the resolved atmospheric flow and the parameterized cloud-microphysical processes (Satoh et al., 2019; Stevens et al., 2020). Moreover, and importantly, high-resolution models and satellite observations probe the atmosphere on similar spatial and temporal scales, allowing for a meaningful comparison between simulation and observations that helps model evaluation as well as the interpretation of observations (Satoh et al., 2019). As such, high-resolution modeling might break the so-called cloud parameterization “deadlock” (Randall et al., 2003) and promises to lead to more reliable simulations of cloud and precipitation responses to future climate change (Collins et al., 2018; Roberts et al., 2018; Stevens et al., 2020).

Motivated by these advances, we consider the radiative effects of mid-latitude cloud systems in simulations with a large range of horizontal resolutions, with three different treatments of atmospheric convection and with two different treatments of cloud microphysics in this study. This creates a hierarchy of simulations that at the one end resembles current low-resolution climate models with parameterized convection and relatively simple cloud microphysics and at the other end resembles the next-generation high-resolution models with explicit convection and more detailed cloud microphysics. Through this approach we investigate how a sequential reduction in model grid spacing from climate-model scales of 80 down to 2.5 km affects, and hopefully improves, the simulation of cloud-radiative effects. Furthermore, we investigate the impact of subgrid-scale parameterization choices regarding convection (fully explicit convection vs. parameterized shallow convection vs. parameterized convection) and cloud microphysics (one-moment scheme vs. two-moment scheme) on cloud-radiative effects and the radiation budget. To this end we analyze simulations with the ICOSahedral Nonhydrostatic (ICON) model (Zängl et al., 2014) over a large domain of the North Atlantic. Our work contributes to recent efforts to understand the sensitivity of climate simulations with respect to horizontal resolution and convection parameterization (Evans et al., 2017; Haarsma et al., 2016; Maher et al., 2018; Thomas et al., 2018; Vanni ere et al., 2019; Webb et al., 2015). We expand these efforts by bridging the gap between current climate models and convection-permitting models.

The focus region of this study is the mid-latitude North Atlantic. This is motivated on the one hand by its importance for current and future European weather and on the other hand by the difficulties of current coarse-resolution global climate models to represent the radiative effects of mid-latitude clouds (Bodas-Salcedo et al., 2014; Voigt et al., 2019) and their coupling to the circulation (Grise & Polvani, 2014). Cloud-radiative effects in the mid-latitudes feedback onto circulations. As such, they are essential to anticipated poleward shift and strengthening of the eddy-driven jet streams under global warming (Albern et al., 2019; Ceppi & Hartmann, 2016; Li et al., 2019; Voigt & Shaw, 2016), and they also can impact mid-latitude weather on timescales of days (Grise et al., 2019; Sch afer & Voigt, 2018).

Biases in simulated mid-latitude CREs appear to be primarily due to deficiencies in parameterized physics of clouds and convection (Ceppi & Hartmann, 2015). These physics strongly depend on cloud type. Analysis

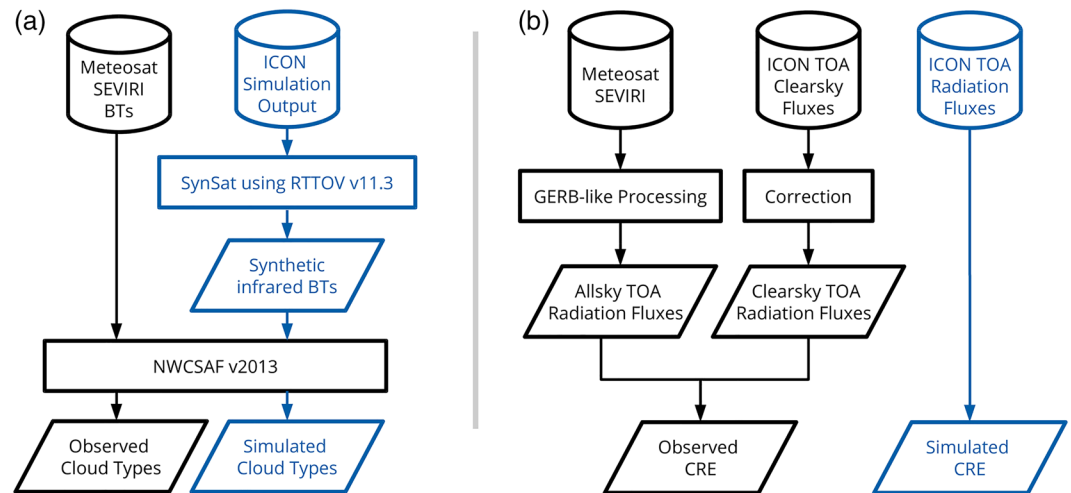


**Figure 1.** Overview of the workflow for (a) the calculation of a consistent cloud classification and (b) the derivation of CREs. Two parallel paths for observations (black) and the simulations (blue) are shown. The symbols in the top row visualize the input data (either satellite data archive or simulation output). Final data are shown in the last row. Rectangles denote processing methods further discussed in the text, and slanted parallelograms correspond to intermediate and final data.

of data from space-born imaging radiometers has shown that low-level clouds over the oceans provide the largest contribution to the net TOA CREs because reflection of sunlight dominates over the trapping of longwave radiation (Chen et al., 2000; Hartmann et al., 1992; Ockert-Bell & Hartmann, 1992). The traditional cloud classification approaches have been revised to assess the importance of cloud regimes as a whole using clustering techniques (McDonald & Parsons, 2018; Oreopoulos et al., 2016; Oreopoulos & Rossow, 2011) and the vertical structure of cloud fields based on active satellite sensors (L'Ecuyer et al., 2019; Stephens et al., 2018). The latter showed that clouds are predominantly organized in multiple layers, which is typically not resolved by passive imagery. Because active satellite observations are very sparse in time and space, we here nevertheless rely on the traditional cloud classification approach to separate cloud cover and CRE model biases into contributions from different cloud types. The comparison is based on instantaneous and high-resolution geostationary satellite data. We follow modern model evaluation standards and sequentially derive synthetic satellite observations using a satellite simulator (similar to Bodas-Salcedo et al., 2011; Matsui et al., 2019; Pincus et al., 2012) and cloud products with an advanced cloud classification software. For the latter step, we apply the cloud classification consistently for the full diurnal cycle (including nighttime). This improves the attribution of instantaneous CREs to different cloud types.

The paper is organized as follows: In section 2, the setup of the ICON model simulations and sensitivity studies is described. Section 2 also provides information on the observed and synthetic narrow-band satellite radiances that are forwarded into the cloud classification software and on our method for deriving TOA radiation fluxes from Meteosat observations. Section 3 presents the main results. We first consider domain-averaged radiation fluxes and CREs and then split cloud cover and radiative effects into contributions from different cloud types. A summary and conclusions are given in section 4. A more detailed description of the modifications of the cloud classification software and supporting information is provided in the supplement.

## 2. Data and Methods

### 2.1. Overview of the Analyses Workflow

Before we provide more details, Figure 1 presents an overview of the workflow and analyses steps for observations (black) and simulations (blue). Used acronyms are listed in Table 1. The diagram is to be read from top to bottom. The input data from Meteosat SEVIRI (see section 2.2) and ICON (see section 2.3) are provided in the first row. From these, observed and simulated cloud types (Figure 1a) and CREs (Figure 1b) are derived, as shown in the last row. Importantly, this workflow makes sure that observations and simulations are directly comparable to each other.

**Table 1**  
*List of Most Important Acronyms*

Acronym	Explanation
BT	Brightness Temperature
CRE	Cloud-Radiative Effect
GERB	Geostationary Earth Radiation Budget
ICON	ICOsahedral Nonhydrostatic
NAWDEX	North Atlantic Waveguide and Downstream impact EXperiment
NWCSAF	Satellite Application Facility in support to NoWCasting and very short range forecasting
RTTOV	Radiative Transfer for Television infrared observation satellite Operational Vertical sounder
RRTM	Rapid Radiation Transfer Model
SEVIRI	Spinning Enhanced Visible and InfraRed Imager
SynSat	Synthetic Satellite imagery
TOA	Top-Of-the-Atmosphere

For cloud classification, ICON simulations are translated into observation space using the SynSat forward operator (section 2.3). Based on observed and synthetic infrared BTs, cloud types are derived with the help of the NWCSAF v2013 software (section 2.4). For the assessment of CREs, Meteosat SEVIRI data are processed to obtain GERB-like all-sky radiation fluxes at the top of the atmosphere (section 2.2). The observed all-sky fluxes are supplemented by simulated clear-sky fluxes, which are corrected with a scaling factor in the shortwave and a constant additive offset in the longwave part to correct for biases in simulated ocean surface properties (section 2.5).

## 2.2. Meteosat Observations

Observations are provided by measurements of the imaging radiometer SEVIRI (Spinning Enhanced Visible and InfraRed Imager) on board the geostationary satellites of the Meteosat Second Generation (MSG) series operated by EUMETSAT (European Organisation for the Exploitation of Meteorological Satellites). We utilize multispectral data from SEVIRI's operational prime service located at a nominal longitude of zero degrees and a nadir resolution of  $3 \times 3 \text{ km}^2$  (Schmetz et al., 2002). An example of upwelling thermal radiation measured at  $10.8 \mu\text{m}$  is provided in Figure 2 (top row). In the atmospheric window at  $10.8 \mu\text{m}$ , atmospheric gases are relatively transparent, and thermal emission mainly originates from the Earth surface, from clouds, or from a combination of the two (in case of semi-transparent or fractional clouds). High BTs typically represent clear regions, whereas low temperatures represent emission from high cirrus clouds. In the scene of Figure 2, a low-pressure system is located in the Atlantic ocean. Its frontal cloud system, seen by the low BTs, extends towards the south and approaches the British Islands. In the western part of this low-pressure system, cold and rather dry air is advected southwards together with marine, low-level clouds that formed within the cold sector.

The Meteosat satellites also carry the broadband radiometer GERB (Harries et al., 2005) for accurate measurements of all-sky TOA radiation fluxes. Unfortunately, during the period of our analysis GERB was in "safe mode" to protect its sensors. We therefore base our TOA radiation flux estimates on SEVIRI data. So-called GERB-like radiation flux products are derived as internal products in the Royal Meteorological Institute of Belgium (RMIB) GERB processing system, which have been retrieved from the RMIB archive for our study. All GERB-like processing steps are explained in detail in Dewitte et al. (2008), and updates on the calibration of SEVIRI data are given in Meirink et al. (2013). The accuracy of the applied narrowband-to-broadband conversion is 3.5% for shortwave fluxes  $F_{\text{sw}}$  and 0.7% for longwave fluxes  $F_{\text{lw}}$  (Clerbaux et al., 2005). For a particular scene type, this error must be considered as a systematic error. For estimates of downwelling shortwave fluxes, temporal variations in the total solar irradiance are taken into account as described in Mekaoui and Dewitte (2008). Throughout the paper, we use a positive-upward convention so that upwelling fluxes are positive and downwelling fluxes are negative (following Stephens, 2005).

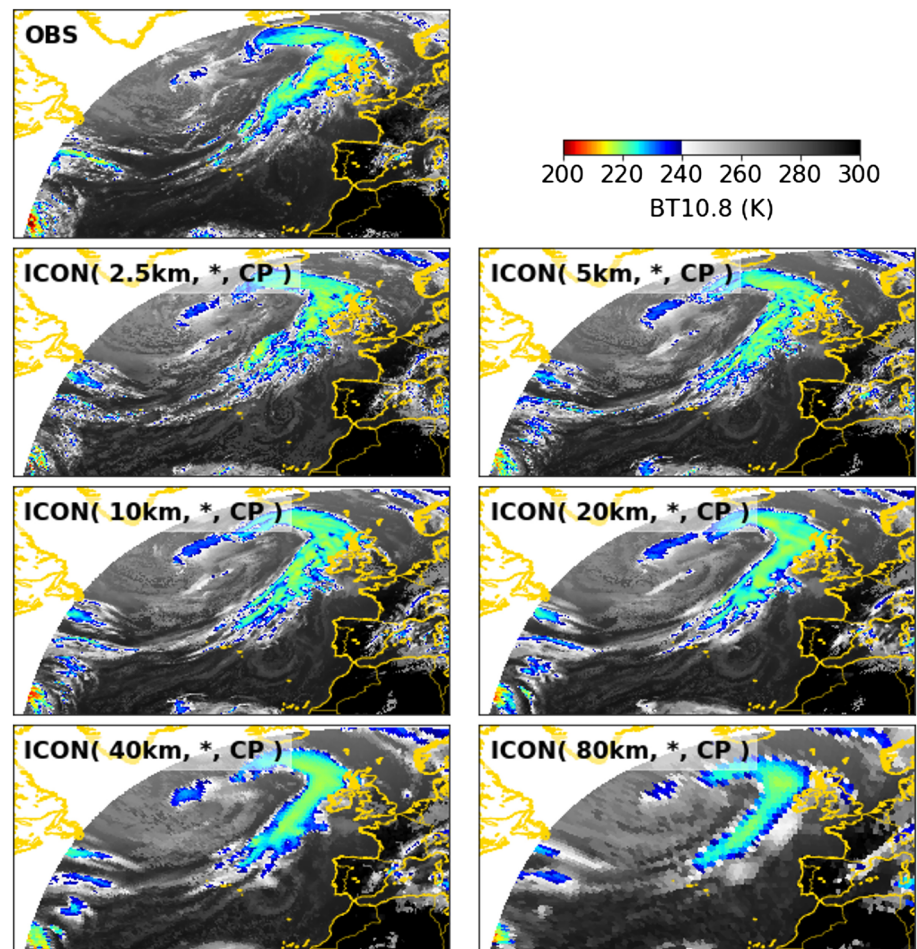


**Figure 2.** Overview of observed and simulated BTs from Meteosat SEVIRI's window channel at  $10.8 \mu\text{m}$  for 1,200 UTC 23 September 2016. Observations are compared to ICON simulations with increasing grid spacing (left to right and downwards, from 2.5 to 80 km). Only the subset of simulation experiments with one-moment microphysics and fully parameterized convection is chosen for visualization. A special color scheme is used to highlight observed and simulated features. BTs over land are also shown to improve anticipation of the cloud scenery. Further analysis however only considers the Atlantic ocean region.

### 2.3. ICON Simulations

We analyze simulations with the ICON model in limited-area setup performed over a large area of the North Atlantic (model version icon-2.1.00 with bug fixes for two-moment cloud microphysics). The simulations were already described in Stevens et al. (2020) (see their Figure 3) and were performed in support to the NAWDEX field campaign of fall 2016 (Schäfler et al., 2018). The domain extends from  $78^\circ\text{W}$  to  $40^\circ\text{E}$  in longitudinal direction and from  $23^\circ\text{N}$  to  $80^\circ\text{N}$  in latitudinal direction. ICON is used with the numerical weather prediction physics package in a setup that largely follows the tropical Atlantic setup of Klocke et al. (2017). ICON is initialized from the Integrated Forecast System (IFS) analysis data of the European Center for Medium-Range Weather Forecasts (ECMWF) at 0 UTC. The lateral boundary data are taken from IFS at 3-hourly resolution. When available, that is, at 0 and 12 UTC, IFS analysis data are used. In between 3-, 6-, and 9-hr IFS forecast data are used. The continually updated analysis and forecast data ensure that the model stays close to the actual meteorology over the simulation period over several days (see below). The IFS data are retrieved at the highest available resolution in space ( $\sim 9$  km horizontal grid spacing). Eleven days are analyzed in total. These result from four simulation sets that each cover a time span of 3 or 4 days and for which the first day is disregarded as spin-up. The simulations are listed in Table 2.

The simulations are performed for six horizontal grid spacings of 80, 40, 20, 10, 5, and 2.5 km. In the vertical, always the same set of 75 levels is used. The thickness of the lowest model layer above ground is

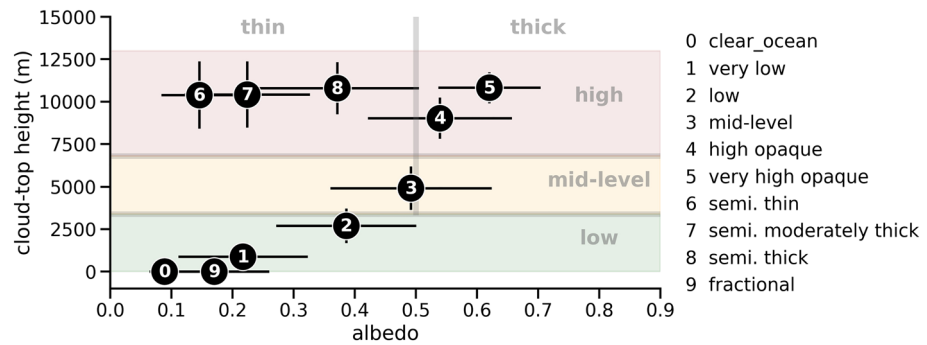


**Figure 3.** Planetary albedo versus cloud-top height for the different NWCSAF classes. The circles represent averages, and the error bars give the standard deviation of clear-sky or cloud properties. Data have been taken from the observed scenery shown in Figures 2 and 4. Numbers  $k = \{0 \dots 9\}$  refer to the different classes listed in the legend. Note that the cloud classes “fractional” and “very low” (which are shown separately here) are combined in the following analysis. For comparison, a second categorization after Hartmann et al. (1992) is provided as background image. It separates cloud amounts into three height categories (low, mid-level, and high) as well as into two opacity levels (thin and thick clouds).

20 m. The model layer thickness increases to  $\approx 100$  m at 1 km altitude above ground up to 1,200 m at the model top of 30 km. Sweeping through the horizontal resolution allows us to cover both the horizontal resolution of present-day global climate models, which typically run at 50–100 km, as well as the resolution of existing convection-permitting regional climate simulations (Prein et al., 2015) and upcoming global simulations (Stevens et al., 2019), which run at 2–5 km. Depending on horizontal resolution, subgrid-scale convection is parameterized following Bechtold et al. (2008) based on the scheme of Tiedtke (1989). When fully enabled, the convection scheme interactively decides on the type of convection to be activated, either deep, mid-level, or shallow convection. For the finest resolution of 2.5 km the convection parameterization scheme is switched off either fully or partly. In the latter setup, only shallow convection is parameterized, whereas mid-level and deep convection are explicitly represented (ICON Model Tutorial April 2018). The setup with only shallow convection parameterization has emerged as the standard setup for 2.5 km-ICON simulations at the German Weather Service (pers. comm. A. Seifert). For resolutions of 5 km and coarser, the convection scheme is fully enabled and takes care of shallow as well as mid-level and deep convection. In addition, for a 3-day subset (22–24 September), the 2.5 km simulations are repeated with fully enabled convection parameterization and the 5 and 10 km simulations with fully disabled convection parameterization. This allows us to compare the impact of the convection scheme with respect to changes in resolution. Besides assessing the impact of resolution and representing convection in an explicit or parameterized manner, we study the impact of representing cloud microphysics. To this end, all simulations are performed with the one-moment cloud microphysical scheme with graupel described in Baldauf et al. (2011) as well as with the two-moment cloud microphysical scheme of Seifert and Beheng (2006). The one-moment scheme is currently used operationally by the German Weather Service; the two-moment scheme is used in large-eddy mode simulations with ICON (Heinze et al., 2017).

To indicate the model setup in the plots and tables, the following nomenclature is used. For instance,  $\text{ICON} ( 10\text{km}, *, \text{CP} )$  refers to ICON simulations with 10 km grid spacing, one-moment microphysics, and fully enabled convection parameterization. In contrast,  $\text{ICON} ( 2.5\text{km}, ** )$  refers to ICON simulations

**Table 2**  
*List of Days Simulated with ICON During the Period of the NAWDEX Field Campaign in Fall 2016*

	Simulation period	Analyzed days	$N_{\text{sim}}$
Set 1	20 September:0UTC–23 September:0UTC	21 and 22 September	14
Set 2	22 September:0UTC–26 September:0UTC	23–25 September	20
Set 3	29 September:0UTC–2 October:0UTC	30 September, 1 and 2 October	14
Set 4	2 October:0UTC–6 October:0UTC	3–5 October	14

Note.  $N_{\text{sim}}$  is the number of simulations as a result of testing for the sensitivity with respect to horizontal resolution and the treatment of cloud microphysics and convection.

**Table 3**  
Overview of Different Treatment of Convection for the Four Sets of Simulations (see Table 2)

	Explicit convection	sCP	CP
Sets 1, 3, 4	2.5 km	2.5 km	5–80 km
Set 2	2.5, 5, 10 km	2.5 km	2.5–80 km
Notation example	ICON ( 2.5km, * )	ICON ( 2.5km, *, sCP )	ICON ( 2.5km, *, CP )

Note. sCP means that only the shallow convection scheme is active. CP means that convection is fully parameterized. A notation example is given in the last row for simulations with 2.5 km grid spacing and one-moment cloud microphysics (indicated by \*; two-moment cloud microphysics are indicated by \*\*).

with 2.5 km grid spacing, two-moment microphysics, and fully disabled convection parameterization—a setup that is called “simulation with explicit convection” in the following. Lastly, ICON ( 2.5km, \*\*, sCP ) refers to a simulation in which only the shallow convection parameterization is enabled. Table 3 summarizes the model setups.

Radiative transfer is calculated by the global model version of the Rapid Radiation Transfer Model, RRTMG (Mlawer et al., 1997). RRTMG uses a reduced number of  $g$ -points ( $g$  is the relative rank of the atmospheric absorption coefficient within a wave length interval) for the correlated  $k$ -method to mitigate some of the computational burden of the parent RRTM model. Fourteen bands are used in the shortwave, and 16 bands are used in the longwave. The solar constant is set to  $1361.4 \text{ W m}^{-2}$ . The diffuse ocean albedo is set to a constant value,  $\alpha_{\text{dif}} = 0.07$ . The direct ocean albedo follows the radiation scheme of Ritter and Geleyn (1992) and is a function of the diffuse albedo and the solar zenith angle,  $\mu_0$ ,

$$\alpha_{\text{dir}} = \frac{1 + 0.5 \cos \mu_0 (\alpha_{\text{dif}}^{-1} - 1)}{(1 + \cos \mu_0 (\alpha_{\text{dif}}^{-1} - 1))^2}. \quad (1)$$

The maximum value allowed for  $\alpha_{\text{dir}}$  is 0.999. The diffuse and the direct ocean albedos are independent of wavelength and do not depend on surface roughness and wind speed. For cloud overlap, the generalized maximum-random overlap scheme of Hogan and Illingworth (2000) is used, with a vertical decorrelation length scale of 2 km. Ozone is specified according to the Global and regional Earth system Monitoring using Satellite and in situ data (GEMS) climatology (Hollingsworth et al., 2008) and aerosol according to the climatology of Tegen et al. (1997). Only aerosol-radiation interactions are considered; aerosol-cloud interactions are not taken into account. The cloud droplet number used in the radiation for the effective radius of droplets and crystals follows a prescribed vertical profile taken from the global atmosphere model ECHAM6 (Stevens et al., 2013). Cloud optical properties, that is, single scattering albedo, extinction coefficient, and asymmetry factor, are also specified as in ECHAM6. Radiation is called every 12 minutes. The radiation fields are output every hour and are always consistent with the simulated cloud field, insolation, solar zenith angle, and the state of the atmosphere and surface. Simulated radiation fluxes were re-gridded onto the observational grid (section 2.2). The analysis is restricted to ocean areas free from sea ice, which avoids complications from differences in surface albedo. As such, the analysis domain includes the North Atlantic and connected water bodies, including the North sea and the Baltic sea (see, for example, Figures 2 and 4). The southern boundary is at  $28.3^\circ\text{N}$  and is determined by the boundary nudging zone of the 80 km grid. A maximum satellite zenith angle of  $75^\circ$  marks the northern boundary of the domain.

For a fair comparison between observations and simulations, the simulated data have to be transformed into the observational space using forward operators (or sometimes called instrument simulators). This has become a standard approach in the last decades (Chaboureaud et al., 2000; Morcrette, 1991; Roca et al., 1997) and is especially important when such ambiguous variables like cloud cover and cloud types are taken into consideration (e.g., Pincus et al., 2012). For our study, we apply the so-called SynSat operator after Keil et al. (2006) and Senf and Deneke (2017) to derive synthetic satellite images with the sensor characteristics of MSG SEVIRI. The SynSat operator prepares vertical profiles of atmospheric temperature, humidity, condensate content, and subgrid-scale cloud cover as well as several surface variables to perform single-column radiative transfer calculations with the RTTOV model (Matricardi et al., 2004; Saunders et al., 1999), here version 11.3. Radiative transfer calculations are performed for different streams per vertical column, which are combined using the maximum-random overlap assumption. We apply a standard configuration that has

been operationally employed by the German Weather Service for several years and utilized for ICON simulations in previous studies (Heinze et al., 2017; Pscheidt et al., 2019; Senf et al., 2018). For this, diagnostic subgrid-scale cloud condensate content is added to its grid-scale counterpart, and ice and snow masses are simply combined to a frozen condensate content. Radiative properties of frozen condensate are estimated using relations for randomly oriented hexagonal columns after Fu (1996) and McFarquhar et al. (2003). The derivation of synthetic BTs is impacted by uncertainties in the formulation of microphysical and radiative hydrometeor properties. A complicating fact is that different model parameterization handles hydrometeor properties differently leading to model-internal inconsistencies as additional cause for uncertainties in the forward calculations. Considering these issues and typical parameter variations, Senf and Deneke (2017) showed that uncertainties in BTs are in the order of a few Kelvin and largest for semi-transparent cirrus clouds with low cloud-top temperatures and with emissivities close to 0.5.

Figure 2 also provides a sequence of synthetic BTs for different model grid spacings from 2.5 to 80 km. As expected, the simulations capture the general cloud scenery and the synoptic-scale features very well. All simulations show the frontal cloud band that approaches the European continent and the upper-level trough located upstream in the North Atlantic. The coarser the resolution, the less detail can be seen in the synthetic BT-fields. However, no abrupt quality changes appear to happen with increased grid spacing.

#### 2.4. Cloud Classification

A cloud classification is derived from simulation and satellite data with the NWCSAF software version 2013. As input, the NWCSAF software expects multispectral data of MSG SEVIRI in its native data format. Using a set of several multispectral tests, a categorical classification is derived for all pixels classified as cloudy (Derrien & Le Gléau, 2005). The applied thresholds mainly depend on the illumination, the viewing geometry, the geographical location, and numerical forecast data describing the moisture and thermodynamic structure at coarser resolution. For the latter, short-term IFS forecasts are supplied.

Cloud types are mainly distinguished by their cloud-top height and opacity similar to the ISCCP-approach (International Satellite Cloud Climatology Project, see e.g. Rossow & Schiffer, 1999). No further distinction between convective and stratiform cloud structures is performed. The typical properties of the NWCSAF cloud types are shown in Figure 3 and contrasted to the categorization after Hartmann et al. (1992). For practical reasons, we consider planetary albedo instead of cloud-optical thickness as measure of cloud opacity. Clouds are divided into different height classes: Very low, low, mid-level, high, and very high clouds are approximately separated by cloud-top altitudes of 2, 3.5, 6.5, and 9.5 km. These values correspond to pressure levels of 800, 650, 450, and 300 hPa and to environmental temperatures of +8, 0, -18, and -40°C. Therefore, very low and low clouds are purely liquid clouds, mid-level and high cloud categories might contain a mixture of hydrometeor phases, and very high clouds are completely glaciated at cloud top. As shown in Figure 3, the high and very high clouds are further subdivided by different opacity levels and called semi-transparent (semi.) thin, semi. moderately thick, semi. thick cirrus as well as high and very high opaque clouds. We call all these categories together “cirrus clouds.” The very high opaque clouds might also contain deep convective cores and parts of anvils close to upper-level convective outflow. An additional class is used for fractional clouds for which multispectral signatures of clouds and underlying surface are identified. Fractional clouds are typically made of small boundary-layer cumuli. The separation between this and the very-low cloud category is rather artificial. We therefore combine these two classes and end up with eight cloud types that will be utilized for further analysis. No undefined class exists, that is, satellite pixels are either classified as cloud-free ( $k = 0$ ) or cloudy ( $k > 0$ ). Therefore, the total domain-average cloud cover can be estimated from the sum of fractions of the individual cloud types.

For very low/fractional clouds ( $k = 1$  and  $k = 9$  in Figure 3), very low albedo values (close to the clear-sky albedo of  $\sim 0.1$ ) are most probable. This cloud type mainly consists of shallow clouds with low geometrical and optical thicknesses especially due to high sub-pixel variability and considerable clear-sky contributions. For more opaque clouds with higher cloud tops, averaged albedo shifts to higher values. These cloud types have larger vertical and horizontal extent and thus higher cloud-optical thicknesses. A similar shift to higher albedo values is found for semi-transparent cirrus going from semi. thin ( $k = 6$ ) to semi. moderately thick ( $k = 7$ ) to semi. thick ( $k = 8$ ). Cloud-spatial structures and sub-pixel variability might be also an important factor for the albedo of semi-transparent cloud categories.

The NWCSAF software has undergone more than a decade of development and is highly adjusted to the needs of operational forecasters and nowcasting applications. It tries to account for as much information



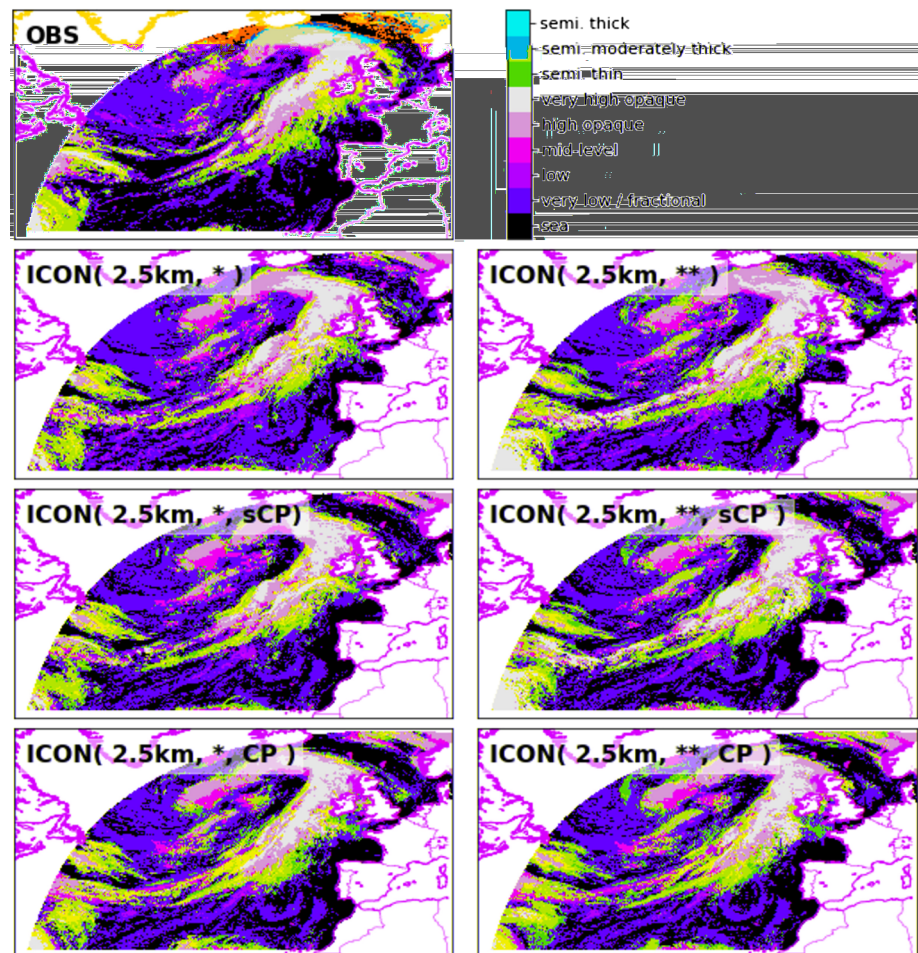


**Figure 4.** Example of observed and simulated cloud types for 1200 UTC 23 Sept 2016 as derived from Meteosat SEVIRI observations (top left) and ICON simulations with 2.5 km horizontal resolution. The left column is for simulations with one-moment cloud microphysics (\*), the right column for simulations with two-moment microphysics (\*\*). The second row is for fully explicit convection, the third row for simulations with a shallow convection scheme (sCP), and the fourth row for simulations with fully parameterized convection (CP).

as available to derive a comprehensive and instantaneous classification of the cloud field. Changes in solar illumination can lead to changes in product quality and systematic differences, especially between daytime and nighttime, are inevitable in the standard setup of the NWCSAF cloud classification. To mitigate these problems and to build a time-consistent cloud classification, we implemented a modification to the cloud product generation chain. The NWCSAF software has been set up to run in permanent-night conditions at which only infrared radiation of terrestrial origin is utilized. We developed an algorithm which reads in infrared SEVIRI radiances from a selected scene and thereafter outputs these data into a template valid for the same day but for 0 UTC. The template files, including the embedded satellite radiances, are supplied to the NWCSAF software which generates a cloud classification in night mode. To keep the software itself unmodified, we provide simple estimates of radiances at  $3.9 \mu\text{m}$  which are mandatory but contaminated with sunlight during daytime (further explained in the supplement). Beyond time consistency, there is another major advantage of our approach: It also allows to exchange real observations with synthetic observations. In our case, we utilized synthetic radiances derived from all the different simulations with the SynSat method (see section 2.3) and provide these data to the NWCSAF software. In this way, a cloud classification is obtained for all simulations that is directly comparable to its observational counterpart.

An example scenery of an instantaneous and high-resolution cloud classification is shown in Figure 4. The scene is similar to the one shown in Figure 2, but here the focus is on 2.5 km simulations with different treatment of convection and cloud microphysics. A frontal cloud band extends from the British Island to the open

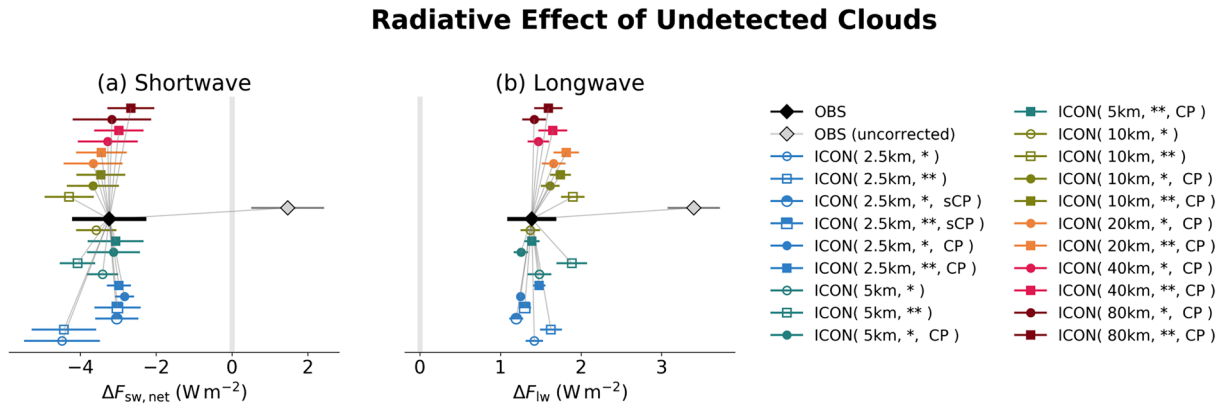


**Figure 5.** The radiative effect of undetected clouds in areas classified as cloud-free (i.e.,  $k = 0$ ). All data points show the average difference between clear-sky and all-sky fluxes for (a) shortwave  $\Delta F_{sw, net} = F_{sw, net, clear} - F_{sw, net}$  and (b) longwave  $\Delta F_{lw} = F_{lw, clear} - F_{lw}$ . The bars give a robust estimate of the standard error of the daily-average values over all simulation sets, thus provide a confidence interval. For this, the difference between the 84th and sixteenth percentile has been calculated to approximate twice the multiday standard deviation  $2\sigma$ , which was further divided by  $\sqrt{N}$  with  $N = 11$  for the all experiments except the additional runs from simulation Set 2 (see Table 3). Colored symbols represent different simulations which have been vertically stacked to improve visibility. The gray symbols show the uncorrected observational estimate, where the all-sky fluxes are based on Meteosat, but the clear-sky fluxes are directly taken from ICON ( 10km, \*, CP ). The black symbols show the corrected observational values with a scale factor applied to the shortwave and a constant additive offset to the longwave part of clear-sky fluxes taken from ICON ( 10km, \*, CP ). Thin gray lines connect all other symbols to the observation for improved interpretation. The clear-sky bias of the simulations is directly obtained from the difference between black and gray symbols.

Atlantic. West of this cold front, marine clouds of type “low” and “very low / fractional” propagate towards the European continent. In the subtropical areas, Meteosat observations show a rather low fraction of low and very low/fractional marine clouds. The amount of these cloud types, which appear in large patches of marine stratocumulus, is strongly overestimated. This is a common bias in all considered ICON simulations at 2.5 km, especially in the variants with explicit convection (see also Senf et al., 2018) and might reflect weaknesses in the setting and coupling of the convection scheme and planetary-boundary layer scheme.

### 2.5. Estimation of Observed Clear-Sky Radiation Fluxes

We are interested in the cloud impact on broadband shortwave and longwave radiation fluxes. This impact is commonly measured in terms of cloud-radiative effects (CREs),

$$CRE_{net} = \overline{F_{net, clear}} - \overline{F_{net}}, \quad (2)$$

which are defined as time-average difference between hypothetical clear-sky fluxes that would occur in the absence of clouds and cloud-affected all-sky fluxes. We follow the sign convention of Stephens (2005) and remind the reader that we defined upwelling all-sky and clear-sky fluxes as positive. Positive CREs indicate a gain of radiative energy and a warming effect of clouds; negative CREs indicate a loss of radiative energy and a cooling effect. Note that CREs are the net result of different cloud types; the radiative impact of individual cloud types is analyzed later in section 3.2.

The ICON simulations provide all-sky and clear-sky fluxes, where the latter are calculated via a second radiation call with cloud fields set to zero. Simulated CREs follow directly from the application of equation 2. Deriving clear-sky fluxes for the observations is more difficult. Observational clear-sky fluxes could be estimated from all-sky fluxes in regions classified as cloud-free, but these might contain undetected clouds and could be biased toward drier and more stable atmospheric conditions (Sohn et al., 2010). For our analysis the situation is even more challenging because (i) the North Atlantic is very cloudy, and (ii) we are interested in instantaneous high-resolution radiation fluxes and CREs for which the clear-sky fluxes cannot be derived by temporal and spatial aggregation (as done in, e.g., Futyán & Russell, 2005). We therefore apply the following recipe to estimate observational clear-sky fluxes (clear-sky path in Figure 1b):

- (i) Clear-sky fluxes are taken from simulations as first guess (similar to Allan, 2011). The ICON ( 10km, \*, CP ) experiment has been chosen as reference.
- (ii) A bias correction is applied to simulated clear-sky fluxes under the constraint that the *radiative effects of undetected clouds have similar magnitudes in observations and simulations*.

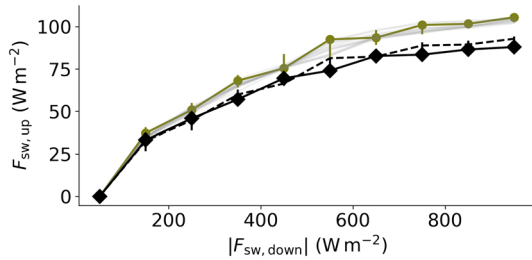


**Figure 6.** Simulated and observed upwelling versus downwelling shortwave fluxes in cloud-free areas. The upwelling flux is calculated for 10 bins of the downwelling flux. Symbols denote conditional median values, and error bars show the inter-quartile range. Simulations are shown in gray, with the simulations for ICON ( 10km, \*, CP ) shown in olive green. Observations are shown by the black diamonds and the black solid line. The dashed black line shows the upwelling flux from ICON ( 10km, \*, CP ) rescaled by a factor of 0.88.

The second step is based on the fact that for ICON simulations, differences between clear-sky and all-sky radiation fluxes are also available for regions that are classified as cloud-free ( $k = 0$ ). As shown in Figure 5, these differences are not zero and are caused by undetected clouds. We thus need to distinguish between all-sky and clear-sky fluxes in cloud-free regions. Therefore, a distinction between “cloud-free” and “clear-sky” is made throughout the rest of the paper.

The radiative effects of undetected clouds help us to establish a bias correction to translate simulated clear-sky fluxes into observational estimates (see also supplement) and to assess the quality of the NWCSAF cloud detection (modified by us to run in night mode). For a perfect cloud classification, all values should be at zero. This is not the case, however, and this demonstrates that a small amount of clouds remains undetected. Undetected clouds from the simulations contribute around  $3 \text{ W m}^{-2}$  of additional shortwave reflection in cloud-free regions (Figure 5a). In the longwave, simulated flux differences are between  $1$  and  $2 \text{ W m}^{-2}$  in

cloud-free regions (Figure 5b) and result from the reduced emission temperature of undetected clouds. The shortwave and longwave effects of undetected clouds partially cancel. When weighted by the fraction of cloud-free areas of around 25%, we conclude that CREs of undetected clouds have negligible impact on the total domain-average radiation budget.

Figure 5 additionally shows two observational estimates of the effects of undetected clouds: One just takes uncorrected (first-guess) ICON clear-sky fluxes (gray symbols), and the other one uses bias-corrected ICON clear-sky fluxes (black symbols). It can be seen that the bias correction brings the observational estimates close to the simulations. The bias correction reduces the first-guess clear-sky fluxes by  $4\text{--}6 \text{ W m}^{-2}$  in the shortwave and by  $2 \text{ W m}^{-2}$  in the longwave. We believe the overestimation in the shortwave results from a too bright ocean surface albedo in ICON. Additional support for this interpretation comes from independent internal investigations by the German Weather Service (pers. comm. A. Seifert). Moreover, simulated ocean surface seems to be too warm causing an overestimation of outgoing longwave clear-sky fluxes that adds to the shortwave bias.

Technically, an offset of  $2 \text{ W m}^{-2}$  is subtracted from  $F_{\text{lw, clear}}$  as simple bias correction in the longwave. For the shortwave, it is more appropriate to apply a scaling factor to the upwelling flux  $F_{\text{sw, up, clear}}$  (see Figure 6). A scaling factor of 0.88 brings the ICON curve approximately down to the observational curve. Figure 6 also shows that all ICON simulations lie together closely. It is therefore of minor importance which ICON experiment is chosen as reference. After correction, the simulated clear-sky fluxes are used together with observed all-sky fluxes for the calculation of observed CREs using equation 2. In summary, the applied strategy for cloud classification is extremely helpful to establish a consistent bias correction of instantaneous clear-sky fluxes estimated from simulations.

### 3. Results

#### 3.1. Domain- and Time-Averaged Radiation Fluxes and Cloud-Radiative Effects

The domain- and time-average radiation fluxes and CREs are discussed first before the dependence of CREs on cloud type is explored in section 3.2. We begin with a comparison of observed and simulated radiation fluxes averaged over the North Atlantic domain and all days (Figure 7). The observed net flux is around  $25 \text{ W m}^{-2}$  and directed outward (Figure 7a), implying that at this time of the year the North Atlantic region loses more radiative energy than it gains. All simulations show larger net fluxes, indicating that they overestimate the loss of radiative energy. Simulations with partly or fully parameterized convection have a net flux of around  $30 \text{ W m}^{-2}$ , with the coarsest resolution showing the smallest deviation with respect to observations. Furthermore, simulations with fully parameterized convection have net fluxes slightly closer to the observation when using one-moment microphysics instead of two-moment microphysics. This might reflect previous model tuning that was done for one-moment but not for two-moment microphysics. Simulations with parameterized shallow convection show net fluxes very similar to simulations with fully parameterized convection. Much stronger deviations occur, however, for simulations with explicit convection for which the net flux reaches about  $40 \text{ W m}^{-2}$ . We note that the deviations in the net flux are not simply a result of

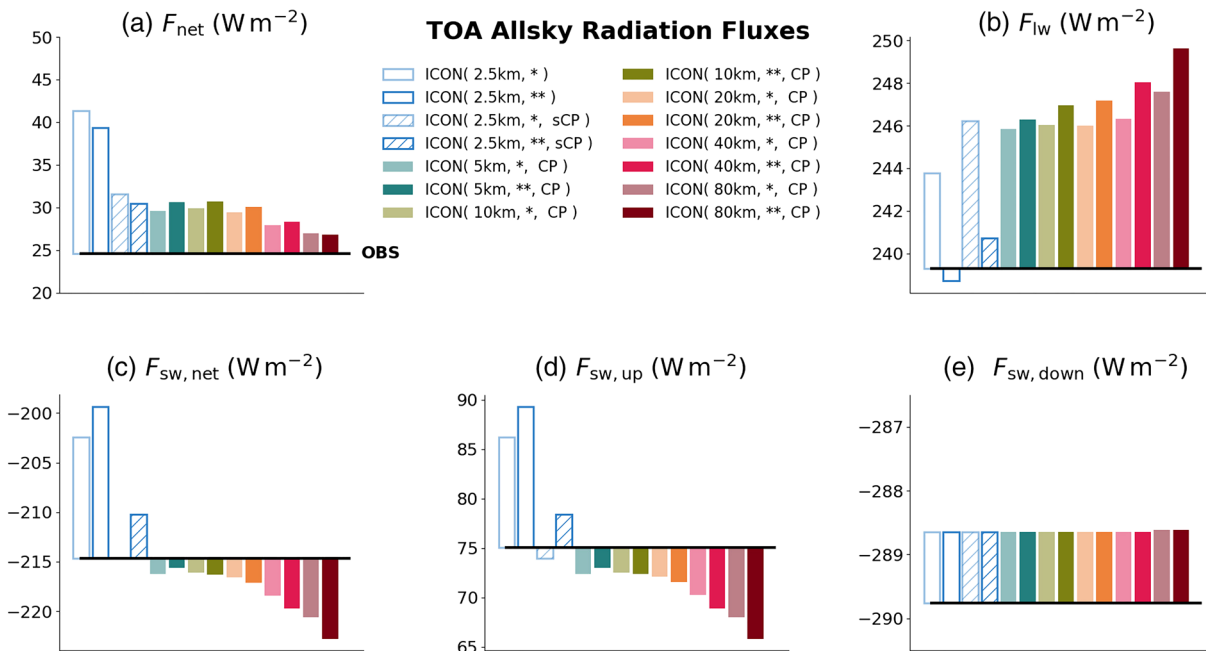


**Figure 7.** Domain and time-averaged all-sky radiation fluxes: (a) total net flux, (b) outgoing longwave flux, (c) net shortwave flux, (d) upwelling shortwave flux, and (e) downwelling shortwave flux. Observations are shown by the black horizontal lines. The deviations of simulated fluxes with respect to observations are shown by colored bars.

differences in the downwelling shortwave flux, which amount to  $1 \text{ W m}^{-2}$  due to slight differences in the solar constant in the simulations and observations.

The better agreement in terms of the net flux for low-resolution simulations and for simulations with (partly) parameterized convection results from compensating biases in outgoing longwave fluxes and upwelling shortwave fluxes (Figures 7b and 7d). These compensating radiation flux biases are a known problem of a large number of climate models, where tuning was aimed in particular at the net TOA energy balance (Klein et al., 2013). With one exception, the simulations overestimate outgoing longwave radiation (Figure 7b), which corresponds to a too high effective emission temperature. The longwave bias increases with increasing grid spacing, with the largest bias found for the coarsest simulation at 80 km resolution. Simulations with fully parameterized convection underestimate upwelling shortwave radiation, which corresponds to a too low planetary albedo. Similar to the longwave bias, the shortwave bias is stronger for the coarser simulations. The better agreement in the net flux found for the coarser simulations is thus achieved for the wrong reason: a systematic bias compensation between longwave and shortwave fluxes that increases when a coarser resolution is used. Put differently, this also means that bias compensation becomes smaller as the resolution is made finer—an encouraging signature of convergence with increasing resolution. Similarly, Hohenegger et al. (2020) found that net shortwave TOA radiation shows a continuous improvement for successive grid refinements in their global ICON simulations with explicit convection.

For the highest resolution simulations at 2.5 km the outgoing longwave flux improves when the shallow-convection scheme is disabled so that convection becomes fully explicit. This is in particular the case for two-moment microphysics, which agrees best with observations in terms of the longwave flux (Figure 7b). However, the simulations with fully explicit convection strongly overestimate the upwelling shortwave flux. As a result, the overall most satisfying agreement is found for simulations that combine two-moment microphysics and parameterized shallow convection. The shallow-convection parameterization avoids the strong overestimation of upwelling shortwave flux found for fully explicit convection.

The simulation of domain- and time-averaged CREs and cloud cover is analyzed in Figure 8. For the observations, CREs are around  $-41 \text{ W m}^{-2}$  in the shortwave and around  $27 \text{ W m}^{-2}$  in the longwave, with a net cooling effect of clouds of  $-14 \text{ W m}^{-2}$ . These CRE values are in the same range as global and long-term averaged observations. However, in the seasonal mean, twice as large CRE values would be found for the North Atlantic region (Zelinka et al., 2017). Simulated shortwave and longwave CREs are negatively correlated,

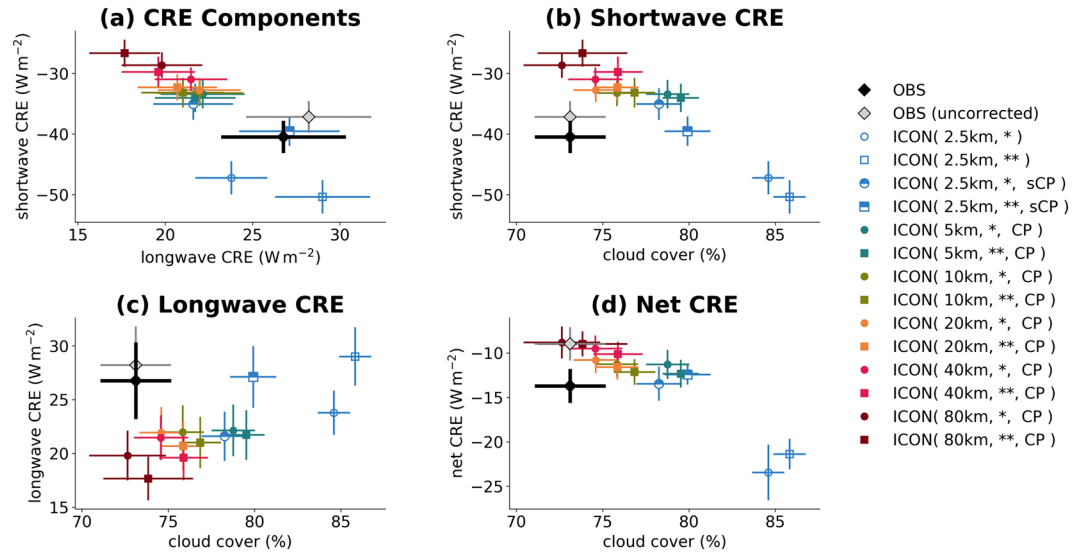


**Figure 8.** Comparison of domain- and time-averaged cloud-radiative effects and cloud cover: (a) longwave CRE versus shortwave CRE. Cloud cover versus (b) shortwave CRE, (c) longwave CRE, and (d) net CRE. Similar to Figure 5, symbols denote average values, and error bars provide confidence intervals. Please note the differences in the y-axis range.

with more positive longwave CREs obtained for more negative shortwave CREs (Figure 8a). Simulations with fully parameterized convection lie in the upper left quadrant of Figure 8a and thus underestimate the magnitude of both longwave and shortwave CREs. Although these simulations show some improvement with decreasing grid spacing, none of the simulations approaches the observed CREs, and the impact of resolution appears to saturate at grid spacings between 10 and 20 km. This indicates that even if the grid spacing was further reduced, the simulations would be unable to approach the observations if convection is fully parameterized. This idea is supported by Figure S5 (supporting information).

In contrast, simulations with shallow-convection scheme or with fully explicit convection are scattered around the observations (Figure 8a). In these simulations, the impact of grid-scale cloud microphysics is also much more pronounced. This is because less or no subgrid-scale cloud condensate is produced by the convection parameterization, which has its own and much simpler convection microphysics description. Overall, this suggests a clear benefit from (partly) disabling the convection scheme. In fact, simulations with shallow-convection scheme and two-moment microphysics show a remarkable match with observed longwave and shortwave CREs.

Figures 8b–8d further show the relation between CREs and cloud cover. In the observations, cloud cover is around 73%. Cloud cover is a primary control on CREs (e.g., Dolinar et al., 2015). Unsurprisingly, this is visible in the simulations, which show a near-linear relation between cloud cover and the CREs. In part, this clear relation is due to the fact that the analyses were only made for one particular model, the ICON model. Greater spread would be expected for the comparison of several models with different parameterizations (see Nam et al., 2012). For our analysis, the observations do not fall onto the simulation-based relationship. This leads to a dilemma: For none of the simulations do CREs and cloud cover at the same time match the observations. Cloud cover is better simulated for coarser grid spacings, whereas CREs improve as the grid spacing is refined. This indicates that the distribution of cloud-optical thicknesses and, associated with this, the vertical cloud structure is insufficiently represented in ICON.

Using equation 2 the radiation flux biases of the ICON simulations with respect to observations can be written as the sum of clear-sky and CRE biases, that is,

$$\delta \bar{F} = \bar{F}_{\text{ICON}} - \bar{F}_{\text{OBS}} = \delta \bar{F}_{\text{clear}} - \delta \text{CRE}. \quad (3)$$

The results of this decomposition are collected in Figure 9, with net flux biases shown in the left column, shortwave flux biases in the middle column, and longwave flux biases in the right column. The matrix presentation of Figure 9 allows for two implicit summing rules: The left column is the sum of the middle and

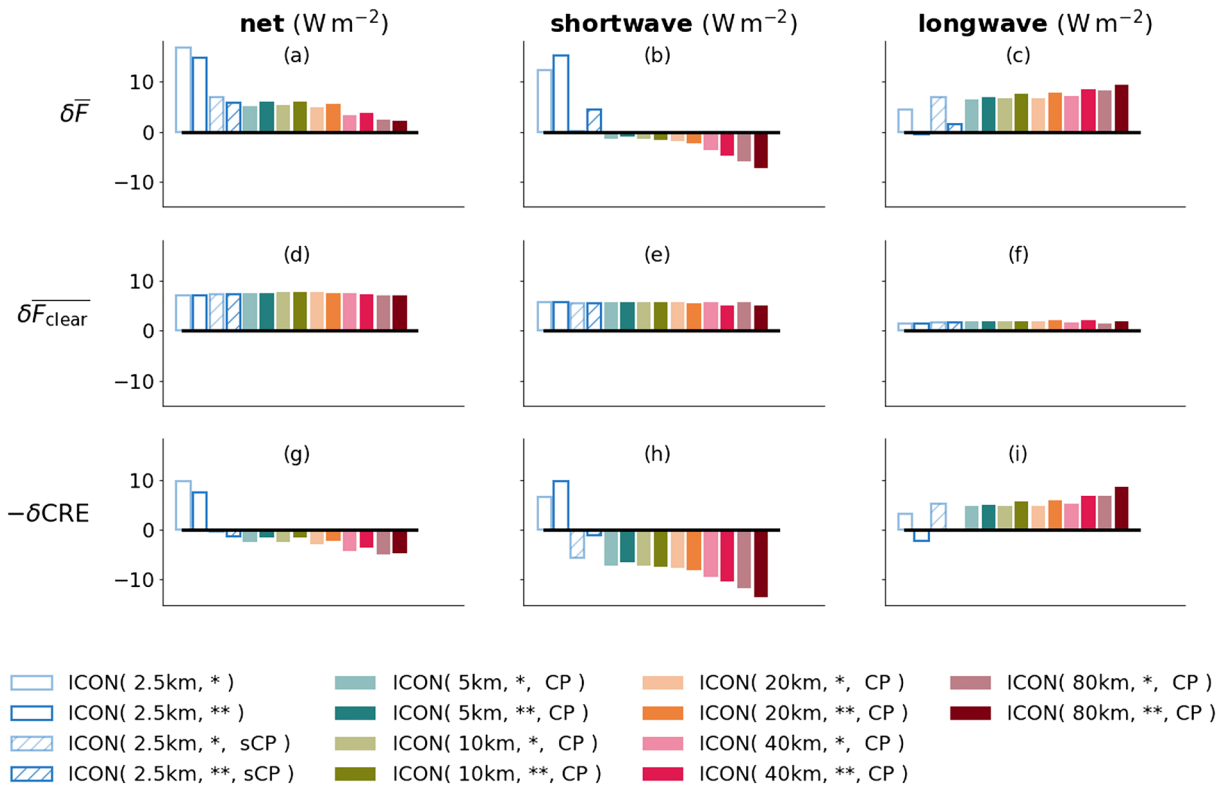


**Figure 9.** Decomposition of domain- and time-averaged biases for net (left), shortwave (middle), and outgoing longwave (right) radiation fluxes. The all-sky bias (first row) is the sum of clear-sky (second row), and CRE (third row) biases. The clear-sky biases are calculated with respect to the bias-corrected clear-sky fluxes of ICON ( 10km, \*, CP ), which serves as observational reference.

right columns, and the first row is the sum of second and third rows. The second row of Figure 9 shows that net biases are to a substantial extent due to clear-sky biases, which are independent of the simulation setup and amount to  $\sim 7.4 \text{ W m}^{-2}$ . The biases in simulated clear-sky fluxes have already been identified in section 2.5 where a correction for observational clear-sky estimates was constructed. The clear-sky bias mostly arises from the shortwave ( $\sim 5.6 \text{ W m}^{-2}$ ), with a smaller longwave contribution ( $\sim 1.8 \text{ W m}^{-2}$ ). The magnitude of the clear-sky shortwave bias is somewhat surprising and likely reflects an imperfect representation of ocean surface albedo in the ICON simulations.

The dependence of all-sky flux biases on resolution and the treatment of convection and cloud microphysics results entirely from CREs (Figure 9, third row). The net CRE bias counteracts the clear-sky bias and thus reduces the net all-sky bias for simulations with fully parameterized convection. For simulations with fully explicit convection, the net CRE bias adds to the clear-sky bias and therefore increases the net all-sky radiation bias. For simulations with parameterized shallow convection, the CRE biases depend on cloud microphysics. With one-moment microphysics, the CRE biases are similar to the biases found for fully parameterized convection. In contrast, with two-moment microphysics there is essentially no CRE bias, neither in the shortwave, longwave, nor net. The net flux bias of the two-moment simulation with parameterized shallow convection is therefore entirely due to clear-sky biases, which could be decreased by adjusting the ocean albedo.

The above analyses have already shown that CRE biases become smaller when the spatial resolution of ICON is refined. This effect is quantified more precisely in Figure 10 which shows the resulting CRE biases and their changes for simulation Set 2 (see Table 3). For Set 2, additional simulations are available, which allow to assess the effect of grid refinement on CRE biases simulated with explicit convection. The magnitudes of shortwave CRE biases become smaller for refining grid spacing from 10 to 2.5 km and explicit convection (Figure 10a). The sign of the longwave CRE bias depends on the choice of the microphysics scheme. For a detailed assessment of the resolution impact, simulation pairs were formed in which one simulation has half the grid spacing of the other simulation. Microphysics and convection parameterization were chosen

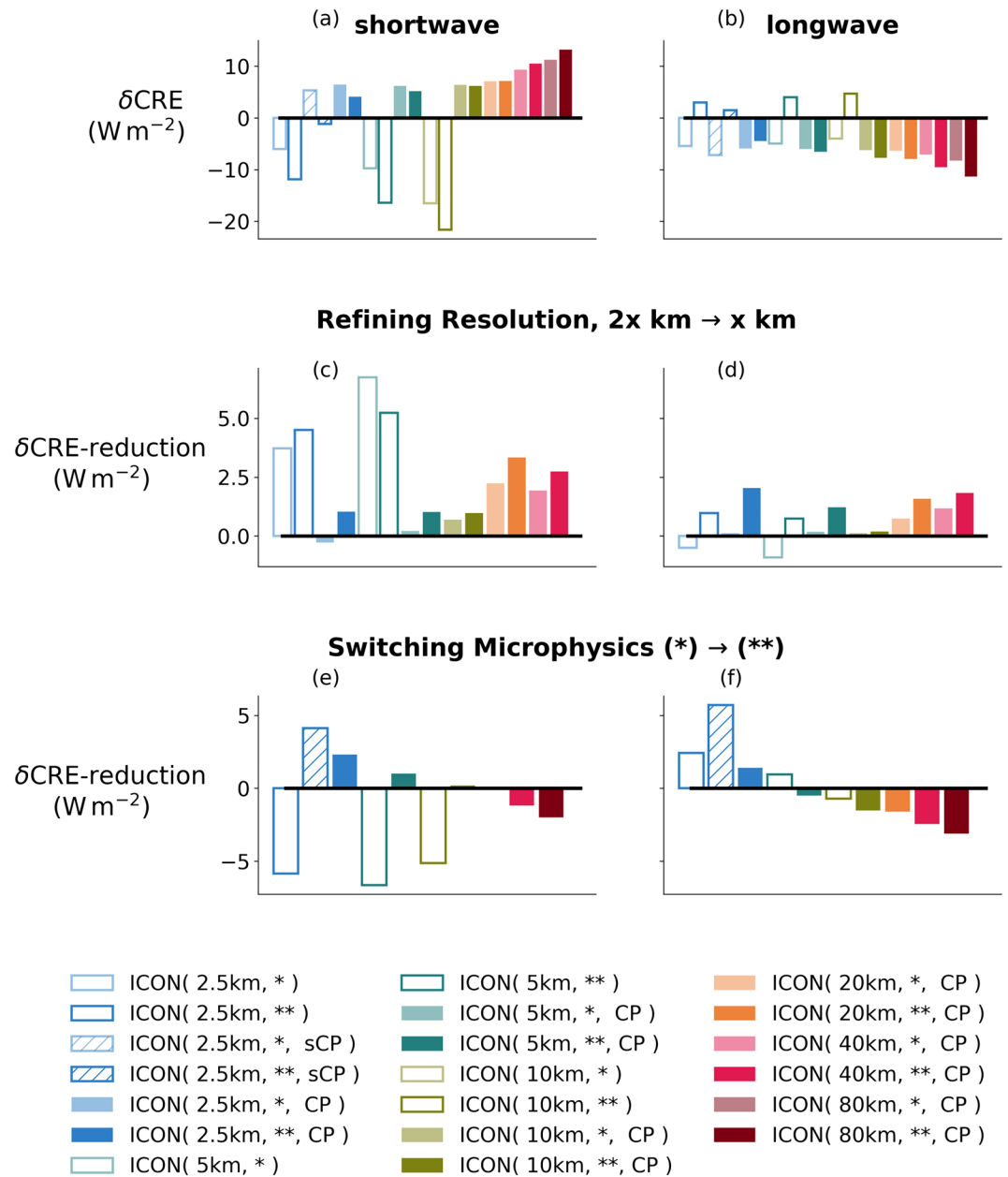


**Figure 10.** Impact of resolution and microphysics on CRE biases. Similar to Figures 9h and 9i, CRE biases are shown for shortwave (left) and longwave (right) but only for simulation Set 2 (see Table 3). Additionally, it is shown how CRE biases are reduced when resolution is refined (middle row) and microphysics is switched from the one-moment scheme to the two-moment scheme (bottom row). All other parameters were set equal, and the ICON experiment, to which it is switched, is indicated in colored bars. A reduction of the CRE bias is shown with positive and an increase with negative values.

identically. Absolute values of the CRE biases were subtracted from each other in such a way that a positive value indicates an improvement by grid refinement. It can be seen that refining resolution always improves shortwave CRE biases (Figure 10c). The improvement is less pronounced for grid spacings less than 20 km and fully parameterized convection. However, when using explicit convection, the refinement down to 2.5 km leads to a substantial reduction of shortwave CRE biases. For the longwave, the behavior is different (Figure 10d). Simulations with fully parameterized convection and two-moment microphysics experience continuous improvement with each refinement step down to 2.5 km. In contrast, longwave CRE biases simulated with explicit convection and one-moment microphysics become even worse when horizontal resolution is refined. As a further analysis, simulation pairs were formed using those with the same

resolution and convection parameters but different microphysics. Positive changes in CRE biases indicate improvements when switching to two-moment microphysics (Figures 10e and 10f). For coarse resolutions, switching to two-moment microphysics leads to worse CRE biases in the longwave and in the shortwave. For smaller grid spacing and partly or fully parameterized convection, the sign changes and switching to two-moment microphysics can now lead to substantial improvements. For simulations with fully explicit convection, these improvement of CRE biases are only found in the longwave whereas switching microphysics causes unexpectedly increased biases in the shortwave. The clarification of the exact causes for the parameter dependencies found here requires further investigations.

### 3.2. Dependence of Cloud-Radiative Effects and Cloud Cover on Cloud Type

We now explore the origins of the domain- and time-averaged cloud cover and CRE biases in the ICON simulations. To this end we use the cloud classification outlined in section 2.4, which allows us to quantify the biases as a function of cloud type. This is done by writing the instantaneous domain-averaged net flux,  $F_{\text{net}}$ , as a sum of contributions from the  $K$  cloud types of the cloud classification,

$$F_{\text{net}} = \sum_{k=0}^K f_k F_{\text{net},k}, \quad (4)$$

where  $f_k$  is the fractional cloud cover of a certain cloud type  $k$  and  $F_{\text{net},k}$  is the instantaneous net flux averaged over the area covered by cloud type  $k$ . Areas classified as cloud-free are included at  $k = 0$ . As before a positive sign indicates upwelling fluxes. Instantaneous domain- and time-averaged CREs are decomposed analogously,

$$\text{CRE}_{\text{net}} = - \sum_{k=0}^K f_k (F_{\text{net},k} - F_{\text{net,clear},k}), \quad (5)$$

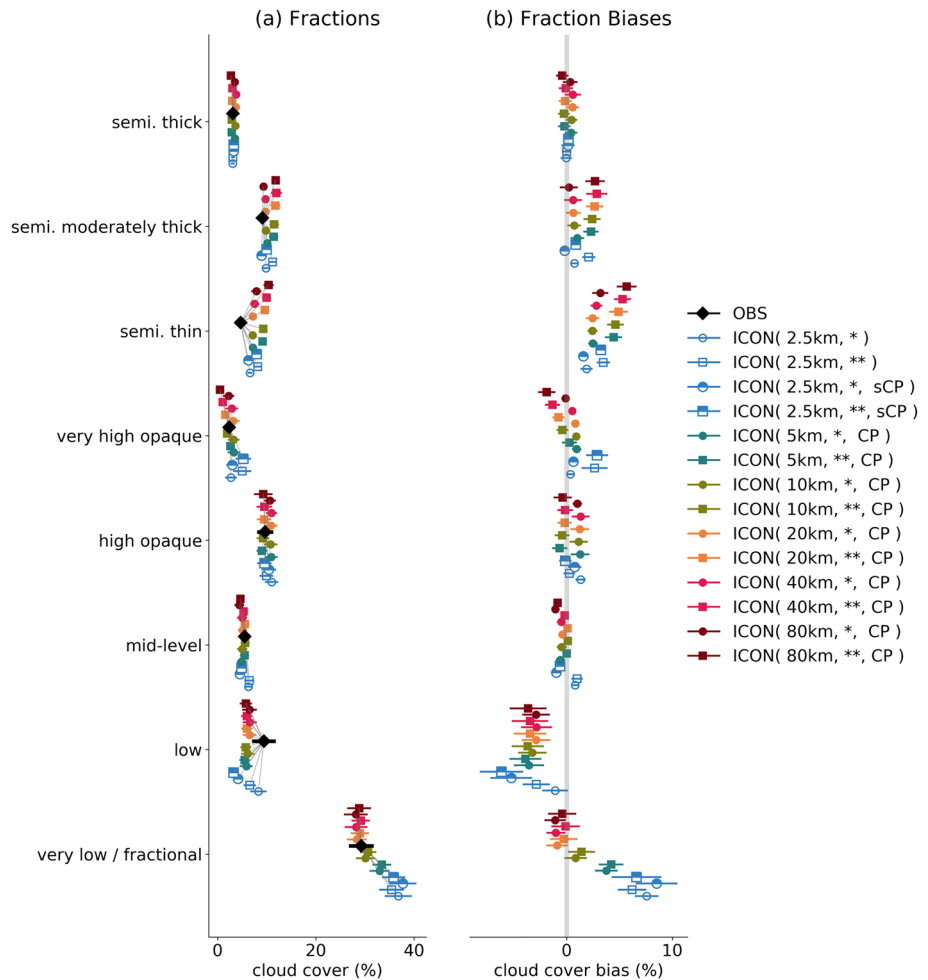
where the cloud type-separated instantaneous net fluxes are averaged over time. This yields to a CRE decomposition into contributions from different cloud types. Note that clear-sky and cloud-free fluxes are not equal,  $F_{\text{net},0} \neq F_{\text{net,clear},0}$ , because of clouds that are undetected by the cloud classification (cf. Figure 5).

Figure 11 presents the cloud-type separation of total cloud cover. In the observations, cloud cover is dominated by very low/fractional clouds, which contribute around 30% to the total observed cloud cover of 73%. The three cloud types “low,” “high opaque,” and “semi. moderately thick” clouds each provide around 10%. The remaining cloud types are less important. From a qualitative point of view, all simulations capture the cloud cover of the different cloud types rather well. A few features of simulated cloud types, however, stand out:

- (i) The cloud cover of very low/fractional clouds strongly depends on resolution and is better simulated in coarse-resolution simulations with grid spacings between 10 and 80 km. Finer-resolution simulations substantially overestimate very low/fractional cloud cover, with a more severe overestimation as the grid spacing is decreased. The largest overestimation is found for simulations with shallow or fully explicit convection.
- (ii) Most simulations underestimate the low cloud cover and overestimate the cloud cover of semi-transparent clouds. These biases are less resolution dependent and become smaller when convection is fully explicit.
- (iii) The choice of the microphysics scheme (one-moment vs. two-moment scheme) has a dominant impact on the cloud cover of cirrus clouds, which are represented by the five cloud types “high” and “very high opaque” as well as “semi. thin,” “semi. moderately thick,” and “semi. thick.” The effect is evident for high and very high opaque clouds for which the two-moment scheme produces smaller cloud cover than the one-moment scheme for fully parameterized convection but higher cloud cover for very high opaque clouds and parameterized shallow convection. At the same time, the two-moment scheme leads to increased cloud cover and cloud-cover biases for semi. thin and moderately thick clouds independent of the treatment of convection.

An overestimation of marine shallow cloud cover has already been observed in Senf et al. (2018), where ICON simulations were performed at 2.5 km grid spacing and with fully explicit convection. This persistent bias can also be found here and is a problem especially for simulated cloud coverage in the subtropical regions (see Figure 4). A grid spacing of 2.5 km is still too coarse, so that the cloud-scale circulations are not





**Figure 11.** Observed and simulated cloud cover as a function of cloud type (a) as well as cloud cover biases of the simulations with respect to Meteosat observations (b). Similar to Figure 5, symbols denote average values and error bars provide confidence intervals.

sufficiently resolved. As result, too large and too regular structures of marine stratocumulus appear in the simulations.

To understand the microphysical sensitivity of the simulated cirrus clouds, it must be considered that the microphysics scheme in ICON was inherited from the weather model of the Consortium for Small-scale Modeling (COSMO). For COSMO a systematic overestimation of the cirrus cover was found (Böhme et al., 2011; Senf & Deneke, 2017). In order to eliminate this error, adjustments were made in the description of ice microphysics which reduce the optical thickness of cirrus clouds (Eikenberg et al., 2015; Köhler & Seifert, 2015). In the ICON simulations presented here, this may lead to a situation where semi-transparent cirrus is more overestimated by the two-moment scheme.

The domain- and time-averaged shortwave CRE depends on the typical albedo of a certain cloud type (see Figure 3). This relation is further illustrated by Figure 12a where CREs have been calculated for a hypothetical overcast situation in which the radiative effect of each cloud type was considered separately assuming a total coverage of 100%. Based on observations, very low/fractional clouds induce a rather low shortwave overcast CRE of  $-30 \text{ W m}^{-2}$ . The shortwave overcast CRE increases reaching  $-140 \text{ W m}^{-2}$  for very high, opaque clouds. The concurrent increase of albedo and cloud-top height also leads to increases in longwave overcast CREs. The imperfect compensation between shortwave and longwave CREs causes net effects that have different signs for observed opaque and observed semi-transparent cirrus clouds. All opaque clouds induce a net cooling due to their negative net CREs in the observation. For observed low and mid-level clouds, the magnitudes of net overcast CREs are largest with  $-50 \text{ W m}^{-2}$ . The warming effect of observed

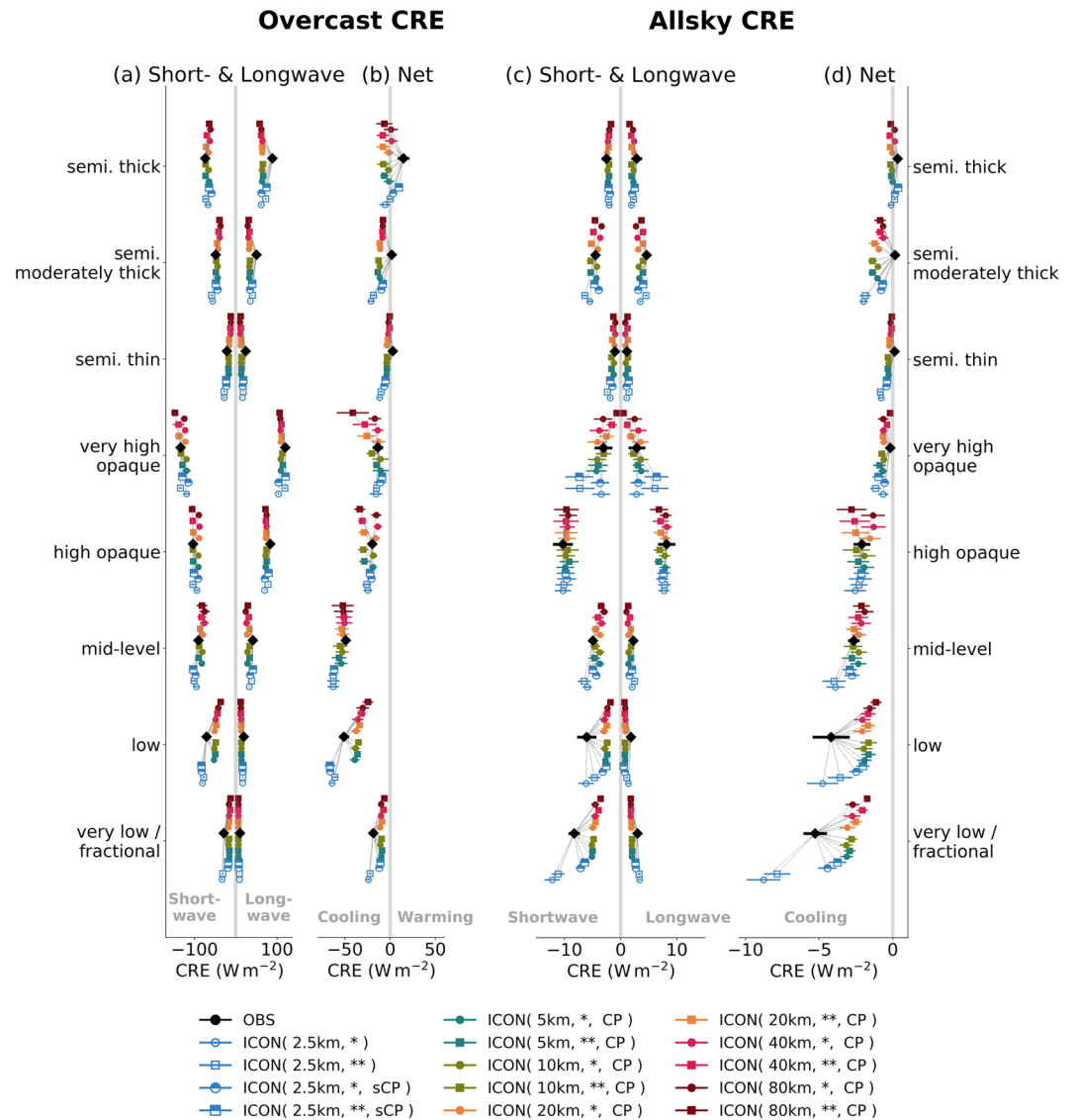


**Figure 12.** Observed and simulated (a, b) overcast CREs and (c, d) all-sky CREs for different cloud types. Overcast CREs are calculated assuming a hypothetical cloud cover of 100%. All-sky CREs include weighting by the cloud-type’s specific cloud cover. Similar to Figure 5, symbols denote average values and error bars provide confidence intervals.

semi-transparent clouds is less pronounced and is largest for semi. thick clouds with  $15 \text{ W m}^{-2}$ . These numbers are consistent with the findings of Chen et al. (2000) who attribute the largest negative shortwave CRE to their deep convective cloud type (comparable with our opaque very high category) and who also find a positive net CRE for their cirrus cloud type (comparable to our semi-transparent thin category).

The comparison of observed overcast CREs with their simulated counterparts helps to assess how good the different simulation setups represent the individual cloud-type specific radiation fluxes (independently of the fractional cloud cover of each type). On a qualitative level, all simulations perform very well showing the observed dependence of overcast CREs on cloud type. Most remarkably, none of the simulated semi-transparent cloud types causes significant positive net CREs (except for ICON(2.5 km, \*\*, sCP)), that is, hardly any of the ICON simulations induce a net domain-average warming from semi-transparent cirrus (see Figure 12b). For all simulated semi-transparent cirrus cloud types, the longwave CREs and thus their thermal cloud emissivities are underestimated (see Figure 12a).

The dependence of all-sky CREs on cloud type is presented in Figures 12c and 12d. Following equation 5, all-sky CREs are calculated by weighting the difference between overcast and clear-sky radiation fluxes by

the cloud cover of each cloud type. The relative amount of each cloud type determines the importance of this cloud type and its CREs for the domain- and time-average. Thus, simulated biases in all-sky CREs can arise from biases in (i) the radiative properties of a given cloud type and (ii) the cloud cover of a given cloud type. Biases in radiative properties result from a misrepresentation of the distribution of cloud-optical thickness, which is directly linked to the representation of vertical structure of the cloud type. Cloud-cover biases provide information on the misrepresentation of the horizontal extent of the respective cloud type. From Figure 12d, we infer that mainly the four cloud types “very low/fractional,” “low,” “mid-level,” and “high opaque” (with decreasing importance) contribute to the observed negative net all-sky CREs. The remaining four cloud types either have near zero net overcast CREs or too little cloud cover. For simulations with fully parameterized convection, the magnitudes of net all-sky CREs for very low/fractional and low clouds are severely underestimated. The discrepancy is much reduced for simulations with shallow convection at 2.5 km grid spacing, especially for one-moment microphysics. In contrast, the net all-sky CREs of very low/fractional clouds are overestimated in simulations with fully explicit convection. The all-sky net CREs of mid-level clouds are better represented for simulations with either shallow or full convection scheme than in simulations with fully explicit convection. In addition, semi-moderately thick clouds have too negative all-sky net CREs in all simulations, with the largest bias for simulations with fully explicit convection.

To separate the effects of cloud type-dependent cloud cover and radiative properties on biases of simulated all-sky CREs, we apply a bias decomposition to equation 5,

$$\delta \text{CRE}_{\text{net}} = \underbrace{-\sum_{k=0}^K \delta f_k (F_{\text{net},k} - F_{\text{net,clear},k})}_{\text{cloud cover}} - \underbrace{\sum_{k=0}^K f_k \delta (F_{\text{net},k} - F_{\text{net,clear},k})}_{\text{radiative properties}} - \underbrace{\sum_{k=0}^K \delta f_k \delta (F_{\text{net},k} - F_{\text{net,clear},k})}_{\text{co-variation}}. \quad (6)$$

The first term results from a misrepresentation of cloud cover, the second term from a misrepresentation of radiative properties and overcast CREs, and the third term from the covariation between the two factors. The “cloud cover” term shows how well the horizontal extent is simulated by cloud type. The “radiation flux” term is related to the vertical structure of a cloud type. As before, cloud-free contributions are included at  $k = 0$ . The decomposition holds for the all-sky net CREs as well as its shortwave and longwave components.

Figure 13 summarizes biases in the domain- and time-averaged CREs and their decomposition. As discussed in section 3.1, net CREs are biased negative for simulations with explicit convection, that is, clouds cool too much but biased positive for simulations with shallow-convection scheme and fully parameterized convection (except for ICON (2.5 km, \*, SCP)), that is, clouds cool too little. For the latter simulations, net CRE biases become smaller as the grid spacing is decreased. The compensation of CRE biases originating in the longwave and shortwave is very apparent for fully convection-parameterized simulations (Figures 13a–13c).

The bias compensation between shortwave and longwave CREs leads to different roles of cloud cover and radiative properties, depending on whether one looks at net CREs or their shortwave and longwave components. For net CREs, cloud cover biases dominate. They are responsible for around half of the positive bias for fully parameterized convection (Figure 13d). For simulations with fully explicit convection, in contrast, biases in radiative properties clearly control the net CRE biases. For the shortwave and longwave CRE components, biases in radiative properties dominate in general. A pronounced compensation between shortwave and longwave CRE biases is apparent. We thus find that the earlier discussed compensation of shortwave and longwave flux biases directly traces back to a misrepresentation of cloud-radiative properties. Switching from one-moment to two-moment microphysics has different effects on cloud cover and radiative properties related CRE biases. It is found for nearly all simulations that the shortwave and longwave CRE biases due to radiative properties become smaller. For the coarser simulations, the resulting improvement is more than compensated by biases in the “cloud cover” term. Thus, the CRE biases become larger when switching to the two-moment scheme in these coarser ICON experiments (see also Figures 10e and 10f). The simulations with shallow-convection parameterization possess smaller biases than the fully parameterized simulations. The simulations with fully explicit convection show acceptable results for the longwave bias due to radiative

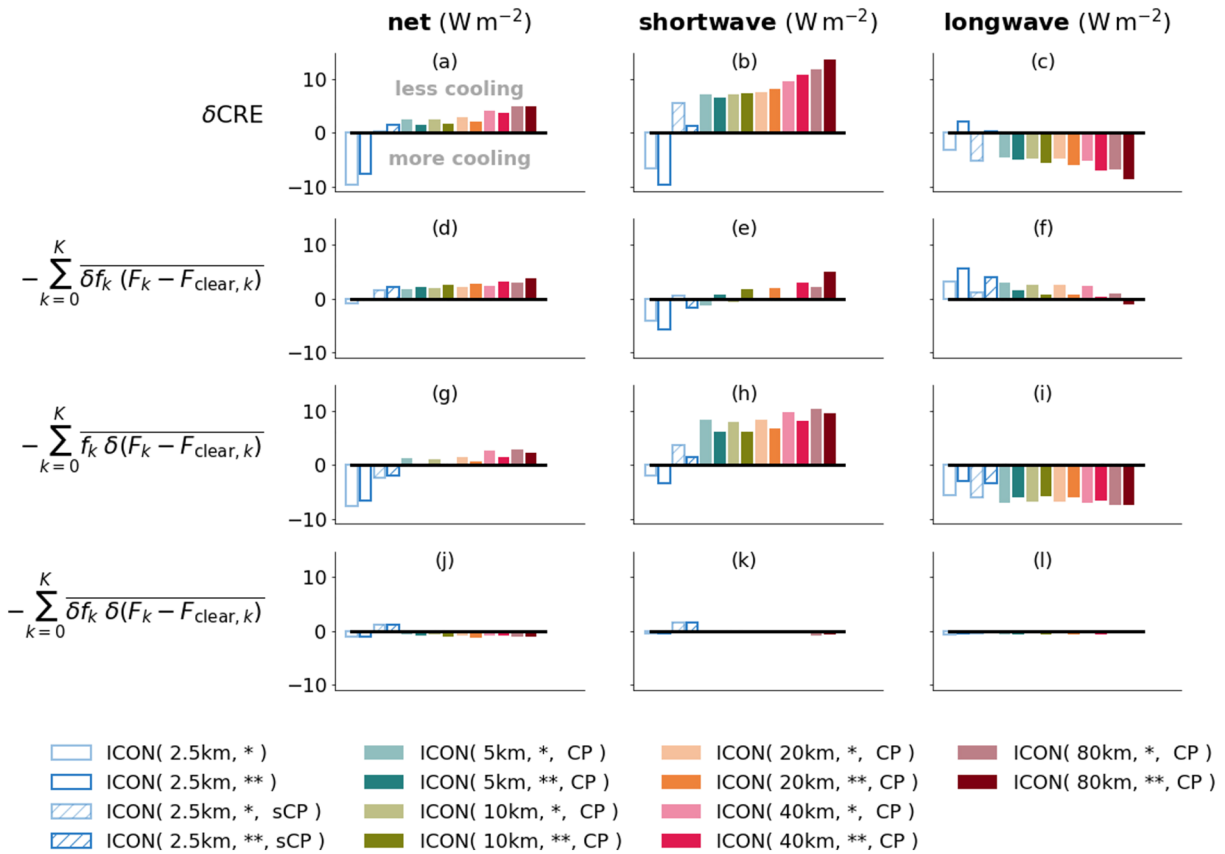


**Figure 13.** Decomposition of CRE biases (first row) into contributions from biases in cloud cover (second row) and cloud-radiative properties (third row). Covariations between biases in cloud cover and radiative properties are shown in the fourth row. The net CRE biases (left column) are decomposed into shortwave and longwave (middle and right columns) contributions.

properties. Their worse net performance originates from the missing compensation by shortwave biases, which are also negative for these simulations.

The interpretation of CRE biases is further supported by Figure 14, which provides a detailed bias decomposition separated by cloud type. We see that not only the compensation between shortwave and longwave CRE biases is important but also the compensation of biases originating from different cloud types (Klein et al., 2013). For the net CRE biases (Figure 14c), mainly cloud types “very low/fractional” and “low” contribute to the positive bias of simulations with fully parameterized convection. This is partially compensated by a negative net CRE bias from semi. moderately thick clouds. When split by cloud type, the net CRE bias of simulations with fully parameterized convection is dominated by CRE biases due to radiative properties.

For shortwave and longwave CRE biases (Figures 14a and 14b), it is found that the resolution dependence of CRE biases not only originates from very low/fractional and low clouds but also from very high opaque clouds. This cloud type is connected to deep convection which representation significantly improves for decreasing grid spacing. Especially, some simulations with two-moment microphysics show a rather poor performance for the very high opaque clouds. The coarse simulation at 80 km underestimates the fractional coverage of this cloud type, in contrast the simulation with shallow convection parameterization at 2.5 km overestimates the fractional coverage of very high opaque clouds (see also Figure 11b). The spatial representation of this cloud type needs to be addressed in future. In the shortwave, the positive CRE bias of simulations with fully parameterized convection mainly comes from very low/fractional and low clouds. For the former, biases in radiative properties dominate whereas for the latter CRE biases due to cloud cover also contribute. Switching from one-moment to two-moment scheme, we find improvements in the representation of shortwave components of individual radiative properties (see Figures 13h and 14g), which indicate that the vertical structure of clouds in terms of optical thicknesses has improved. These improvements are partially masked by worse cloud cover biases (see Figure 13e). In the longwave, many cloud types simulated

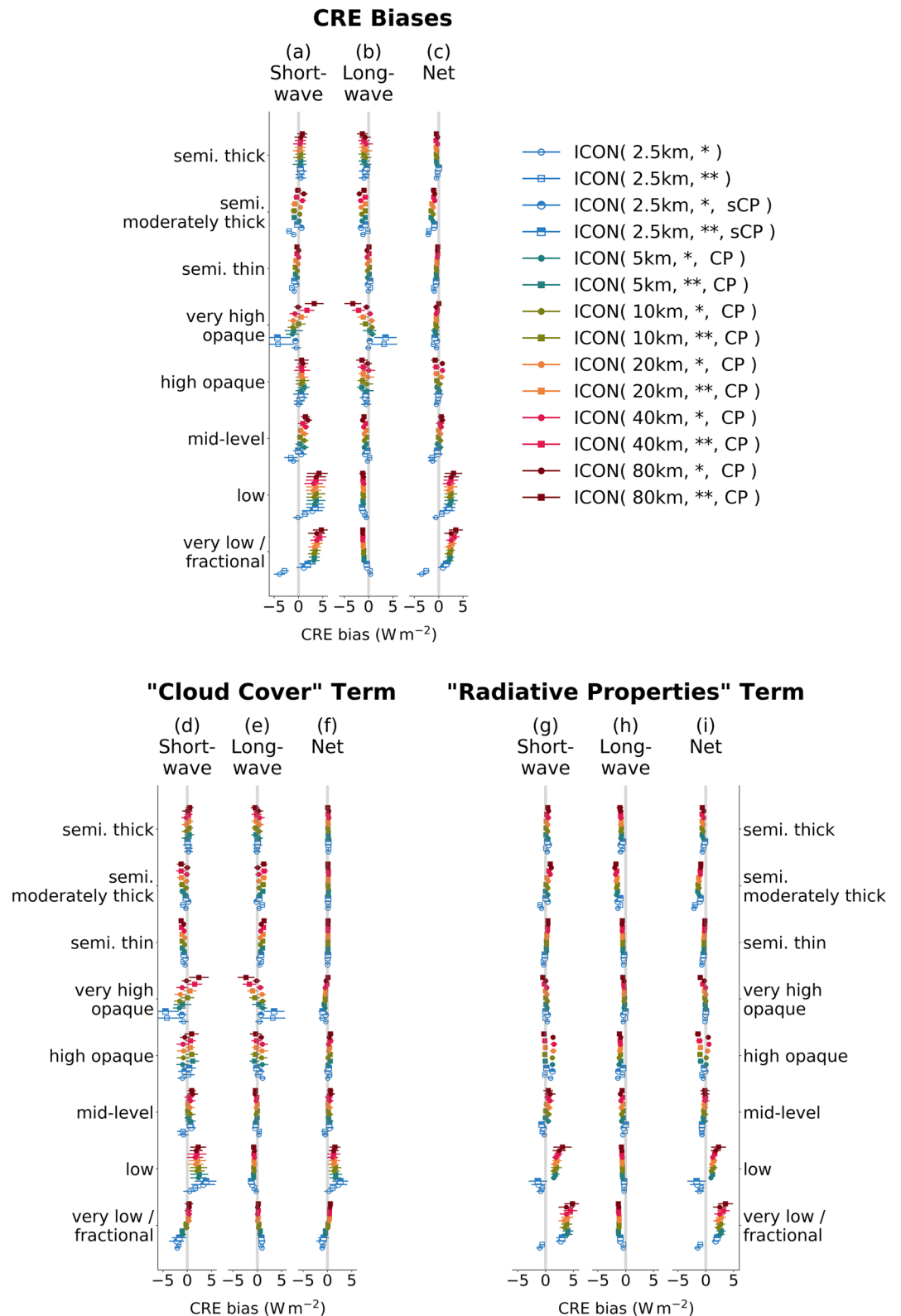


**Figure 14.** CRE biases and their decomposition for different cloud types. Following equation 6, (top row) biases in CREs are separated into (bottom row) contribution from (left) cloud-cover biases and (right) radiation-flux biases. The split into (a, d, and g) shortwave and (b, e, and h) longwave components that sum up to the (c, f, and i) net CRE bias is also provided in the different subpanels. Similar to Figure 5, symbols denote average values, and error bars provide confidence intervals.

with fully parameterized convection show a negative bias originating from the bias in radiative properties. The magnitudes of the individual longwave biases are much smaller for simulations with explicit convection.

In summary, the above analysis showed that future model development should equally concentrate on improvements of simulated clear-sky and cloud-affected TOA radiation fluxes. For the former, we recommend to revise the formulation of ocean albedo to reach better consistency with observations. For CREs, strategies for further improvement depend on the choice of the convection scheme, especially at kilometer-scale resolutions. For simulations with fully parameterized convection, radiation is typically too weakly interacting with clouds, that is, clouds appear too dark and too warm, especially for low and very low/fractional clouds. Hence, in contrast to the well-known “too few, too bright” low-cloud problem of several climate models (Klein et al., 2013; Nam et al., 2012), low and very low clouds in ICON at coarse resolutions need to become brighter. This could be achieved by improving radiative properties of these cloud types, either from a macrophysical or a microphysical point of view. Specifically, in the used ICON version the effective radius of cloud particles taken in the radiative transfer follows from a prescribed number concentration of cloud particles and is unaware of the number concentration simulated by the two-moment microphysics scheme. Adjusting this inconsistency might help to correct the CRE biases, for example, the negative biases in longwave CREs of semi-transparent cirrus. For simulations with only shallow or fully explicit convection, the radiative properties of clouds show signs of improvement. However, ICON with shallow convection simulates very low clouds, which still appear too dark and too similar to the clouds from the fully parameterized convection simulations. To improve the representation of this cloud type, new parameterization approaches need to be explored, such as those using stochastic sampling (Sakradzija & Klocke, 2018). The simulations with explicit convection show a promising convergence, which should be investigated by further refinements down to the hectometer-scale (Stevens et al., 2020).

#### 4. Conclusions and Outlook

Clouds regulate Earth's energy budget (Ramanathan et al., 1989). Shallow low-level clouds are efficient scatterers of shortwave radiation and, in combination with their small thermal contrast to Earth's surface, they have strong negative cloud-radiative effects and cool the Earth. In contrast, the cloud-radiative effects of high-level cirrus clouds also include longwave effects so that depending on cirrus-optical properties these clouds can either have a near zero or a warming effect (Stephens, 2005).

In mid-latitude environments, cyclones lead to the formation of frontal cloud bands with a complicated mixture of stratiform and convective clouds, possibly including multilayer structures and embedded convection. Realistically representing such complex cloud structures and their radiative effects poses a challenge to numerical models, especially over oceans where extended shallow boundary-layer cloud fields occur in addition. Furthermore, the radiative impact of clouds on the mid-latitude circulation might depend on cloud type. We therefore investigated the ability of a specific numerical weather prediction—the ICON model (Zängl et al., 2014)—to represent cloud cover and cloud-radiative effects for selected days of the NAWDEX field campaign in boreal autumn 2016 over a large North Atlantic domain. Using a comprehensive set of sensitivity simulations that vary horizontal grid spacing between 2.5 and 80 km, we identified sensitivities with respect to model resolution. Moreover, we studied the impact of different choices regarding the parameterization of cloud microphysics (one-moment vs. two-moment scheme) and convection (fully parameterized, shallow-convection only, fully explicit). This allowed us to identify strengths and weaknesses of the different model setups, in particular with respect to top-of-atmosphere radiation fluxes and cloud-radiative effects.

To assess the ICON model we made use of multispectral observations from the geostationary Meteosat satellite in two ways. First, we analyzed observational estimates of instantaneous top-of-atmosphere radiation. Second, we derived a detailed multispectral cloud classification from the Meteosat observations. For a consistent comparison between the ICON simulations and the observations, the simulation data were ingested in a satellite forward operator performing radiative transfer calculations to derive synthetic infrared satellite images. This transfer of the simulations to observation space allowed us to subject simulations and observations to the same cloud classification software and to analyze and compare observed and simulated cloud-type fields within the same framework.

In observations, the average net TOA radiation flux over the North Atlantic region and for the selected analysis days is around  $+25 \text{ W m}^{-2}$ , indicating a net energy loss (remember that we adopted a positive-upward convention for radiation fluxes). Clouds substantially contribute to the energy loss and are responsible for

a net cooling of  $-14 \text{ W m}^{-2}$ . Major contributors to the net CRE are shallow clouds of the cloud type “very low/fractional” and “low,” which both contribute around  $-5 \text{ W m}^{-2}$  to the total net CRE. The shallow clouds also account for around half of the total cloud cover of 73%.

The main results of our comparison between observed and ICON simulated radiation fluxes and cloud fields are as follows:

- (i) For all model setups, the domain- and time-averaged net TOA radiation flux is larger than in the observations, independent of resolution and the treatment of cloud microphysics and convection. The ICON model thus overestimates the TOA loss of radiative energy. Simulations with fully parameterized convection underestimate TOA shortwave reflection and overestimate outgoing longwave radiation, that is, seen from space they are too dark and too warm.
- (ii) There is a systematic bias compensation between shortwave reflection and outgoing longwave radiation. The compensation is stronger for coarse-resolution simulations and becomes smaller for finer resolutions. Clear-sky and CRE biases have similar magnitudes, but only CRE biases are sensitive to horizontal resolution and in fact decrease with finer resolution. For fully parameterized-convection simulations, clouds are too weakly interacting with the radiation field leading to positive CRE biases in the shortwave and negative CRE biases in the longwave which partially compensate each other.
- (iii) For none of the ICON setups, a simultaneous match between observed and simulated CREs and total cloud cover is achieved. Cloud cover compares better to observations for coarse resolutions, whereas CREs compare better to observations for finer resolutions.
- (iv) The cloud cover of shallow clouds (types: “very low/fractional” and “low”) strongly depends on resolution. It compares well with observations for coarser resolutions of 10–80 km, but finer resolutions and explicit convection severely overestimate it by up to 50% relative to observations. For simulations with fully parameterized convection, net CRE-biases of shallow clouds are dominated by positive shortwave biases in radiative properties. Biases in shortwave and net CREs are reduced when only shallow convection parameterization is applied. Using explicit convection even switches the sign of the shortwave CRE-biases leading to too bright shallow clouds and too large cloud-induced reflection.
- (v) The choice of the microphysics scheme has dominant impact on cloud cover of cirrus clouds leading to smaller cloud cover for high opaque and very high opaque clouds and larger cloud cover for semi-thin and semi-moderately thick clouds. No pronounced net warming effect is found for simulated semi-transparent clouds. The net CRE bias of semi-transparent clouds is negative and caused by a misrepresentation of cirrus radiative properties, especially in the longwave.

In summary, our analysis shows that refining horizontal resolution allows the ICON model to more accurately represent cloud-radiative effects over the North Atlantic. We found substantial bias compensation between top-of-atmosphere shortwave and longwave radiation fluxes as well as between clear-sky fluxes and cloud-radiative effects. An acceptable net performance of a selected model setup is not at all a guarantor of realistic individual contributions. The best representation of the domain-average longwave and shortwave CREs is achieved when ICON is configured with two-moment cloud microphysics, a shallow-convection scheme (explicit treatment of mid-level and deep convection) and a horizontal resolution of 2.5 km.

At horizontal resolutions of 80 km, which are typical for climate models, we find substantial CRE biases of up to  $10 \text{ W m}^{-2}$  in both, in the shortwave and in the longwave. Subsequent grid refinements to 40 and 20 km lead to smaller CRE biases. However, at higher resolutions only small and insufficient improvements of the simulated shortwave CREs can be achieved by further refinements. This situation changes when the convection scheme is deactivated, and thus, convection is treated explicitly. With fully explicit convection, the simulation of CREs is improved even if refinements are performed at the kilometer scale (and possibly below). However, a resolution of 2.5 km is still too coarse to resolve the shallow clouds and circulation in the marine boundary layer; therefore, the best simulation of average CREs at 2.5 km is achieved with an explicit treatment of mid-level and deep convection but a parameterized treatment of shallow convection. This simulation setup can represent the radiative-properties term in the CRE decomposition in a satisfactory manner for all cloud types except for very low clouds. For this cloud type, improvements in the simulation of cloud-optical thickness and thus vertical structure are needed. Moreover, the 2.5 km setup with parameterized shallow convection shows some deficits with regard to the fractional coverage of cloud types “very high opaque” and “low” which could be an indication that the linking between resolved and parameterized convection has weaknesses in this setup. Compared to fully explicit convection, the use of

a shallow-convection scheme mitigates the otherwise too high fractional coverage of very low clouds and too strong cloud shortwave reflection and at the same time does not affect longwave CRE, which are dominated by high-level clouds. A deeper understanding of the spatial distribution of the CRE biases is needed. A promising approach would be the analysis of the cloud distribution and its radiative effects as a function of meteorological conditions, for example, cloud controlling factors depending on large-scale circulation and vertical velocity regimes.

### Data Availability Statement

The GERB-like data are made freely available to the user community via the RMIB OnLine Shortterm Service (ROLSS, see <ftp://gerb.oma.be>) server, after registration. The primary data of the ICON simulations (run scripts, namelists, scripts for lateral boundary data) are published at KITopen of Karlsruhe Institute of Technology, <https://doi.org/10.5445/IR/1000123695>. Analysis data have been collected at the long-term archive (LTA) of DKRZ and can be assessed online ([https://cera-www.dkrz.de/WDCC/ui/cersearch/entry?acronym=DKRZ\\_LTA\\_834\\_ds00048](https://cera-www.dkrz.de/WDCC/ui/cersearch/entry?acronym=DKRZ_LTA_834_ds00048)). Open science: The analysis source code has been made freely available to improve reproducibility of our results. Basic analysis tools are written in Python and published online (<https://doi.org/10.5281/zenodo.4028394>). The final plots for our paper were done with Jupyter Notebooks which are published online (<https://doi.org/10.5281/zenodo.3952138>).

### Acknowledgments

We thank three reviewers and the editor for the helpful comments which led to significant improvement of the manuscript. Furthermore, we thank Axel Seifert whose comments on an earlier version of this study led to the addition of the shallow convection experiments. FS and AV are supported by the German Ministry of Education and Research (BMBF) and FONA: Research for Sustainable Development ([www.fona.de](http://www.fona.de)). This work contributes to the WCRP's Grand Challenge on Clouds, Circulation, and Climate Sensitivity and the BMBF-funded project HD(CP)<sup>2</sup>: High Definition Clouds and Precipitation for Advancing Climate Prediction. FS acknowledges funding under respective grants 01LK1507C and 01LK1503F, and AV is supported under Grant Agreement 01LK1509A. The ICON simulations were performed by AV at the DKRZ in Hamburg, Germany, which is thanked for its support. We also thank EUMETSAT for producing the SEVIRI data, which have been obtained from the TROPOS satellite data archive.

### References

- Albern, N., Voigt, A., & Pinto, J. G. (2019). Cloud-radiative impact on the regional responses of the midlatitude jet streams and storm tracks to global warming. *Journal of Advances in Modeling Earth Systems*, *11*, 1940–1958. <https://doi.org/10.1029/2018MS001592>
- Allan, R. P. (2011). Combining satellite data and models to estimate cloud radiative effect at the surface and in the atmosphere. *Meteorological Applications*, *18*(3), 324–333.
- Arking, A. (1991). The radiative effects of clouds and their impact on climate. *Bulletin of the American Meteorological Society*, *72*(6), 795–814.
- Baldauf, M., Seifert, A., Förstner, J., Majewski, D., Raschendorfer, M., & Reinhardt, T. (2011). Operational convective-scale numerical weather prediction with the cosmo model: Description and sensitivities. *Monthly Weather Review*, *139*(12), 3887–3905.
- Bechtold, P., Köhler, M., Jung, T., Doblus-Reyes, F., Leutbecher, M., Rodwell, M. J., et al. (2008). Advances in simulating atmospheric variability with the ECMWF model: From synoptic to decadal time-scales. *Quarterly Journal of the Royal Meteorological Society: A journal of the atmospheric sciences, applied meteorology and physical oceanography*, *134*(634), 1337–1351.
- Bodas-Salcedo, A., Webb, M. J., Bony, S., Chepfer, H., Dufresne, J.-L., Klein, S. A., et al. (2011). COSP: Satellite simulation software for model assessment. *Bulletin of the American Meteorological Society*, *92*(8), 1023–1043.
- Bodas-Salcedo, A., Williams, K. D., Ringer, M. A., Beau, I., Cole, J. N. S., Dufresne, J.-L., et al. (2014). Origins of the Solar Radiation Biases over the Southern Ocean in CFMIP2 Models\* *Journal of Climate*, *27*(1), 41–56. <https://doi.org/10.1175/JCLI-D-13-00169.1>
- Böhme, T., Stapelberg, S., Akkermans, T., Crewell, S., Fischer, J., Reinhardt, T., et al. (2011). Long-term evaluation of COSMO forecasting using combined observational data of the GOP period. *Meteor Z*, *20*, 119–132.
- Boucher, O., Randall, D., Artaxo, P., Bretherton, C., Feingold, G., Forster, P., et al. (2013). Clouds and Aerosols. In *Climate Change 2013: The Physical Science Basis. Contribution of Working Group I to the Fifth Assessment Report of the Intergovernmental Panel on Climate Change* (pp. 571–657). Cambridge, United Kingdom and New York, NY, USA: Cambridge University Press.
- Ceppi, P., Briant, F., Zelinka, M. D., & Hartmann, D. L. (2017). Cloud feedback mechanisms and their representation in global climate models. *Wiley Interdisciplinary Reviews Climate Change*, *8*(4), e465.
- Ceppi, P., & Hartmann, D. L. (2015). Connections between clouds, radiation, and midlatitude dynamics: A review. *Current Climate Change Reports*, *1*(2), 94–102.
- Ceppi, P., & Hartmann, D. L. (2016). Clouds and the atmospheric circulation response to warming. *Journal of Climate*, *29*(2), 783–799.
- Ceppi, P., & Shepherd, T. G. (2017). Contributions of climate feedbacks to changes in atmospheric circulation. *Journal of Climate*, *30*(22), 9097–9118. <https://doi.org/10.1175/JCLI-D-17-0189.1>
- Chaboureaud, J.-P., Cammas, J.-P., Mascart, P., Pinty, J.-P., Claud, C., Roca, R., & Morcrette, J.-J. (2000). Evaluation of a cloud system life-cycle simulated by the Meso-NH model during FASTEX using METEOSAT radiances and TOVS-3I cloud retrievals. *Quarterly Journal of the Royal Meteorological Society*, *126*(566), 1735–1750.
- Chen, T., Rossow, W. B., & Zhang, Y. (2000). Radiative effects of cloud-type variations. *Journal of Climate*, *13*(1), 264–286.
- Clerbaux, N., Bertrand, C., Caprion, D., Depaepe, B., Dewitte, S., Gonzalez, L., & Ipe, A. (2005). Narrowband-to-broadband conversions for seviri. In *Proceedings of the 2005 eumetsat meteorological satellite conference* (pp. 351–357). Dubrovnik, Croatia.
- Collins, M., Minobe, S., Barreiro, M., Bordoni, S., Kaspi, Y., Kuwano-Yoshida, A., et al. (2018). Challenges and opportunities for improved understanding of regional climate dynamics. *Nature Climate Change*, *8*(2), 101.
- Derrien, M., & Le Gléau, H. (2005). MSG/SEVIRI cloud mask and type from SAFNWC. *International Journal of Remote Sensing*, *26*, 4707–4732.
- Dewitte, S., Gonzalez, L., Clerbaux, N., Ipe, A., Bertrand, C., & Paepe, B. D. (2008). The geostationary earth radiation budget edition 1 data processing algorithms. *Advances in Space Research*, *41*(11), 1906–1913.
- Dolinar, E. K., Dong, X., Xi, B., Jiang, J. H., & Su, H. (2015). Evaluation of cmip5 simulated clouds and toa radiation budgets using nasa satellite observations. *Climate Dynamics*, *44*(7–8), 2229–2247.
- Eikenberg, S., Khler, C., Seifert, A., & Crewell, S. (2015). How microphysical choices affect simulated infrared brightness temperatures. *Atmospheric Research*, *156*, 6779. <https://doi.org/10.1016/j.atmosres.2014.12.010>
- Evans, S., Marchand, R., Ackerman, T., Donner, L., Golaz, J.-C., & Seman, C. (2017). Diagnosing cloud biases in the gfdl am3 model with atmospheric classification. *Journal of Geophysical Research: Atmospheres*, *122*, 12,827–12,844. <https://doi.org/10.1002/2017JD027163>



- Fu, Q. (1996). An accurate parameterization of the solar radiative properties of cirrus clouds for climate models. *Journal of Climate*, *9*, 2058–2082.
- Futyan, J. M., & Russell, J. E. (2005). Developing clear-sky flux products for the geostationary earth radiation budget experiment. *Journal of Applied Meteorology*, *44*(9), 1361–1374.
- Gottelman, A., & Sherwood, S. C. (2016). Processes responsible for cloud feedback. *Current Climate Change Reports*, *2*(4), 179–189.
- Grise, K. M., Medeiros, B., Benedict, J. J., & Olson, J. G. (2019). Investigating the influence of cloud radiative effects on the extratropical storm tracks. *Geophysical Research Letters*, *46*, 7700–7707. <https://doi.org/10.1029/2019GL083542>
- Grise, K. M., & Polvani, L. M. (2014). Southern Hemisphere cloud-dynamics biases in CMIP5 models and their implications for climate projections. *Journal of Climate*, *27*(15), 6074–6092. <https://doi.org/10.1175/JCLI-D-14-00113.1>
- Haarsma, R. J., Roberts, M. J., Vidale, P. L., Senior, C. A., Bellucci, A., Bao, Q., et al. (2016). High resolution model intercomparison project (highresmip v1.0) for cmip6. *Geoscientific Model Development*, *9*(11), 4185–4208.
- Harries, J. E., Russell, J. E., Hanafin, J. A., Brindley, H., Futyan, J., Rufus, J., et al. (2005). The geostationary earth radiation budget project. *Bulletin of the American Meteorological Society*, *86*(7), 945–960.
- Hartmann, D. L., Ockert-Bell, M. E., & Michelsen, M. L. (1992). The effect of cloud type on earth's energy balance: Global analysis. *Journal of Climate*, *5*(11), 1281–1304.
- Heinze, R., Dipankar, A., Carbajal Henken, C., Moseley, C., Sourdeval, O., Trömel, S., et al. (2017). Large-eddy simulations over germany using ICON: A comprehensive evaluation. *Quarterly Journal of the Royal Meteorological Society*, *143*(702), 69–100.
- Henderson, D. S., L'Ecuyer, T., Stephens, G., Partain, P., & Sekiguchi, M. (2013). A multisensor perspective on the radiative impacts of clouds and aerosols. *Journal of Applied Meteorology and Climatology*, *52*(4), 853–871.
- Hogan, R. J., & Illingworth, A. J. (2000). Deriving cloud overlap statistics from radar. *Quarterly Journal of the Royal Meteorological Society*, *126*(569), 2903–2909.
- Hohenegger, C., Kornbluh, L., Klocke, D., Becker, T., Cioni, G., Engels, J. F., et al. (2020). Climate statistics in global simulations of the atmosphere, from 80 to 2.5 km grid spacing. *Journal of the Meteorological Society of Japan*, *98*(1), 73–91.
- Hollingsworth, A., Engelen, R. J., Textor, C., Benedetti, A., Boucher, O., Chevallier, F., et al. (2008). Toward a monitoring and forecasting system for atmospheric composition: The GEMS Project. *Bulletin of the American Meteorological Society*, *89*(8), 1147–1164. <https://doi.org/10.1175/2008BAMS2355.1>
- Keil, C., Tafferner, A., & Reinhardt, T. (2006). Synthetic satellite imagery in the Lokal-Modell. *Atmospheric Research*, *82*, 19–25.
- Klein, S. A., Zhang, Y., Zelinka, M. D., Pincus, R., Boyle, J., & Gleckler, P. J. (2013). Are climate model simulations of clouds improving? an evaluation using the isccp simulator. *Journal of Geophysical Research: Atmospheres*, *118*, 1329–1342. <https://doi.org/10.1002/jgrd.50141>
- Klocke, D., Brueck, M., Hohenegger, C., & Stevens, B. (2017). Rediscovery of the doldrums in storm-resolving simulations over the tropical Atlantic. *Nature Geoscience*, *10*(12), 891–896.
- Köhler, C. G., & Seifert, A. (2015). Identifying sensitivities for cirrus modelling using a two-moment two-mode bulk microphysics scheme. *Tellus B*, *67*, 1–27. <https://doi.org/10.3402/tellusb.v67.24494>
- L'Ecuyer, T. S., Hang, Y., Matus, A. V., & Wang, Z. (2019). Reassessing the effect of cloud type on earth's energy balance in the age of active spaceborne observations. part i: Top of atmosphere and surface. *Journal of Climate*, *32*(19), 6197–6217.
- Li, Y., Thompson, D. W. J., Bony, S., & Merlis, T. M. (2019). Thermodynamic control on the poleward shift of the extratropical jet in climate change simulations: The role of rising high clouds and their radiative effects. *Journal of Climate*, *32*(3), 917–934. <https://doi.org/10.1175/JCLI-D-18-0417.1>
- Maher, P., Vallis, G. K., Sherwood, S. C., Webb, M. J., & Sansom, P. G. (2018). The impact of parameterized convection on climatological precipitation in atmospheric global climate models. *Geophysical Research Letters*, *45*, 3728–3736. <https://doi.org/10.1002/2017GL076826>
- Matricardi, M., Chevallier, F., Kelly, G., & Thépaut, J.-N. (2004). An improved general fast radiative transfer model for the assimilation of radiance observations. *Quarterly Journal of the Royal Meteorological Society*, *130*, 153–173.
- Matsui, T., Dolan, B., Rutledge, S. A., Tao, W.-K., Iguchi, T., Barnum, J., & Lang, S. E. (2019). Polaris: A polarimetric radar retrieval and instrument simulator. *Journal of Geophysical Research: Atmospheres*, *124*, 4634–4657. <https://doi.org/10.1029/2018JD028317>
- McDonald, A. J., & Parsons, S. (2018). A comparison of cloud classification methodologies: Differences between cloud and dynamical regimes. *Journal of Geophysical Research: Atmospheres*, *123*, 11,173–11,193. <https://doi.org/10.1029/2018JD028595>
- McFarquhar, G. M., Iacobellis, S., & Somerville, R. C. J. (2003). SCM simulations of tropical ice clouds using observationally based parameterizations of microphysics. *Journal of Climate*, *16*(11), 1643–1664.
- Meirink, J. F., Roebeling, R. A., & Stammes, P. (2013). Inter-calibration of polar imager solar channels using seviri. *Atmospheric Measurement Techniques*, *6*(9), 2495–2508.
- Mekaoui, S., & Dewitte, S. (2008). Total solar irradiance measurement and modelling during Cycle 23. *Solar Physics*, *247*(1), 203–216.
- Mlawer, E. J., Taubman, S. J., Brown, P. D., Iacono, M. J., & Clough, S. A. (1997). Radiative transfer for inhomogeneous atmospheres: RRTM, a validated correlated-k model for the longwave. *Journal of Geophysical Research*, *102*(D14), 16,663–16,682.
- Morcrette, J.-J. (1991). Evaluation of model-generated cloudiness: Satellite-observed and model-generated diurnal variability of brightness temperature. *Monthly Weather Review*, *119*(5), 1205–1224.
- Nam, C., Bony, S., Dufresne, J.-L., & Chepfer, H. (2012). The “too few, too bright” tropical low-cloud problem in cmip5 models. *Geophysical Research Letters*, *39*, L21801. <https://doi.org/10.1029/2012GL053421>
- Ockert-Bell, M. E., & Hartmann, D. L. (1992). The effect of cloud type on earth's energy balance: Results for selected regions. *Journal of Climate*, *5*(10), 1157–1171.
- Oreopoulos, L., Cho, N., Lee, D., & Kato, S. (2016). Radiative effects of global modis cloud regimes. *Journal of Geophysical Research: Atmospheres*, *121*, 2299–2317. <https://doi.org/10.1002/2015JD024502>
- Oreopoulos, L., & Rossow, W. B. (2011). The cloud radiative effects of international satellite cloud climatology project weather states. *Journal of Geophysical Research*, *116*, D12202. <https://doi.org/10.1029/2010JD015472>
- Pincus, R., Platnick, S., Ackerman, S. A., Hemler, R. S., & Patrick Hofmann, R. J. (2012). Reconciling simulated and observed views of clouds: Modis, isccp, and the limits of instrument simulators. *Journal of Climate*, *25*(13), 4699–4720.
- Prein, A. F., Langhans, W., Fosser, G., Ferrone, A., Ban, N., Goergen, K., et al. (2015). A review on regional convection-permitting climate modeling: Demonstrations, prospects, and challenges. *Reviews of Geophysics*, *53*, 323–361. <https://doi.org/10.1002/2014RG000475>
- Pscheidt, I., Senf, F., Heinze, R., Deneke, H., Trömel, S., & Hohenegger, C. (2019). How organized is deep convection over germany? *Quarterly Journal of the Royal Meteorological Society*, *145*(723), 2366–2384.
- Ramanathan, V. L. R. D., Cess, R. D., Harrison, E. F., Minnis, P., Barkstrom, B. R., Ahmad, E., & Hartmann, D. (1989). Cloud-radiative forcing and climate: Results from the earth radiation budget experiment. *Science*, *243*(4887), 57–63.
- Randall, D., Khairoutdinov, M., Arakawa, A., & Grabowski, W. (2003). Breaking the cloud parameterization deadlock. *Bulletin of the American Meteorological Society*, *84*(11), 1547–1564.

- Ritter, B., & Geleyn, J.-F. (1992). A comprehensive radiation scheme for numerical weather prediction models with potential applications in climate simulations. *Monthly Weather Review*, *120*(2), 303–325.
- Roberts, M. J., Vidale, P. L., Senior, C., Hewitt, H. T., Bates, C., Berthou, S., et al. (2018). The benefits of global high resolution for climate simulation: Process understanding and the enabling of stakeholder decisions at the regional scale. *Bulletin of the American Meteorological Society*, *99*(11), 2341–2359.
- Roca, R., Picon, L., Desbois, M., Le Treut, H., & Morcrette, J.-J. (1997). Direct comparison of meteosat water vapor channel data and general circulation model results. *Geophysical Research Letters*, *24*(2), 147–150.
- Rossov, W. B., & Schiffer, R. A. (1999). Advances in understanding clouds from isccp. *Bulletin of the American Meteorological Society*, *80*(11), 2261–2287.
- Sakradzija, M., & Klocke, D. (2018). Physically constrained stochastic shallow convection in realistic kilometer-scale simulations. *Journal of Advances in Modeling Earth Systems*, *10*, 2755–2776. <https://doi.org/10.1029/2018MS001358>
- Satoh, M., Noda, A. T., Seiki, T., Chen, Y.-W., Kodama, C., Yamada, Y., et al. (2018). Toward reduction of the uncertainties in climate sensitivity due to cloud processes using a global non-hydrostatic atmospheric model. *Progress in Earth and Planetary Science*, *5*(1), 67.
- Satoh, M., Stevens, B., Judt, F., Khairoutdinov, M., Lin, S.-J., Putman, W. M., & Düben, P. (2019). Global cloud-resolving models. *Current Climate Change Reports*.
- Saunders, R., Matricardi, M., & Brunel, P. (1999). An improved for assimilation of satellite radiance observations. *Quarterly Journal of the Royal Meteorological Society*, *125*(556), 1407–1425.
- Schäfer, S. A. K., & Voigt, A. (2018). Radiation weakens idealized midlatitude cyclones. *Geophysical Research Letter*, *45*, 2833–2841. <https://doi.org/10.1002/2017GL076726>
- Schäfler, A., Craig, G., Wernli, H., Arbogast, P., Doyle, J. D., McTaggart-Cowan, R., et al. (2018). The north atlantic waveguide and downstream impact experiment. *Bulletin of the American Meteorological Society*, *99*(8), 1607–1637.
- Schmetz, J., Pili, P., Tjemkes, S., Just, D., Kerkmann, J., Rota, S., & Ratier, A. (2002). An introduction to Meteosat Second Generation (MSG). *Bulletin of the American Meteorological Society*, *83*(7), 977–992.
- Seifert, A., & Beheng, K. D. (2006). A two-moment cloud microphysics parameterization for mixed-phase clouds. Part 1: Model description. *Meteorology and Atmospheric Physics*, *92*(1), 45–66.
- Senf, F., & Deneke, H. (2017). Uncertainties in synthetic meteosat seviri infrared brightness temperatures in the presence of cirrus clouds and implications for evaluation of cloud microphysics. *Atmospheric Research*, *183*, 113–129.
- Senf, F., Klocke, D., & Brueck, M. (2018). Size-resolved evaluation of simulated deep tropical convection. *Monthly Weather Review*, *146*(7), 2161–2182.
- Sohn, B. J., Nakajima, T., Satoh, M., & Jang, H. S. (2010). Impact of different definitions of clear-sky flux on the determination of longwave cloud radiative forcing: NICAM simulation results. *Atmospheric Chemistry and Physics*, *10*(23), 11,641–11,646.
- Stephens, G. L. (2005). Cloud feedbacks in the climate system: A critical review. *Journal of Climate*, *18*(2), 237–273.
- Stephens, G. L., Li, J., Wild, M., Clayson, C. A., Loeb, N., Kato, S., et al. (2012). An update on earth's energy balance in light of the latest global observations. *Nature Geoscience*, *5*(10), 691.
- Stephens, G., Winker, D., Pelon, J., Trepte, C., Vane, D., Yuhua, C., et al. (2018). Cloudsat and calipso within the a-train: Ten years of actively observing the earth system. *Bulletin of the American Meteorological Society*, *99*(3), 569–581.
- Stevens, B., Acquistapace, C., Hansen, A., Heinze, R., Klingner, C., Klocke, D., et al. (2020). Large-eddy and storm resolving models for climate prediction the added value for clouds and precipitation. *Journal of the Meteorological Society of Japan*, *98*(2), 395–435.
- Stevens, B., Giorgetta, M., Esch, M., Mauritsen, T., Crueger, T., Rast, S., et al. (2013). Atmospheric component of the mpi-m earth system model: Echem6. *Journal of Advances in Modeling Earth Systems*, *5*, 146–172. <https://doi.org/10.1002/jame.20015>
- Stevens, B., Satoh, M., Auger, L., Biercamp, J., Bretherton, C. S., Chen, X., et al. (2019). Dyamond: The dynamics of the atmospheric general circulation modeled on non-hydrostatic domains. *Progress in Earth and Planetary Science*, *6*(1), 61.
- Tegen, I., Hollrig, P., Chin, M., Fung, I., Jacob, D., & Penner, J. (1997). Contribution of different aerosol species to the global aerosol extinction optical thickness: Estimates from model results. *Journal of Geophysical Research*, *102*(D20), 23,895–23,915.
- Thomas, M. A., Devasthale, A., Koenigk, T., Wyser, K., Roberts, M., Roberts, C., & Lohmann, K. (2018). A statistical and process oriented evaluation of cloud radiative effects in high resolution global models. *Geoscientific Model Development*, *2018*, 1–30.
- Tiedtke, M. (1989). A comprehensive mass flux scheme for cumulus parameterization in large-scale models. *Monthly Weather Review*, *117*(8), 1779–1800.
- Vannière, B., Demory, M.-E., Vidale, P. L., Schiemann, R., Roberts, M. J., Roberts, C. D., et al. (2019). Multi-model evaluation of the sensitivity of the global energy budget and hydrological cycle to resolution. *Climate Dynamics*, *52*(11), 6817–6846.
- Voigt, A., Albern, N., & Papavasileiou, G. (2019). The atmospheric pathway of the cloud-radiative impact on the circulation response to global warming: Important and uncertain. *Journal of Climate*, *32*(10), 3051–3067. <https://doi.org/10.1175/JCLI-D-18-0810.1>
- Voigt, A., & Shaw, T. A. (2015). Circulation response to warming shaped by radiative changes of clouds and water vapour. *Nature Geoscience*, *8*(2), 102–106. <https://doi.org/10.1038/ngeo2345>
- Voigt, A., & Shaw, T. A. (2016). Impact of regional atmospheric cloud radiative changes on shifts of the extratropical jet stream in response to global warming. *Journal of Climate*, *29*(23), 8399–8421. <https://doi.org/10.1175/JCLI-D-16-0140.1>
- Webb, M. J., Lock, A. P., Bretherton, C. S., Bony, S., Cole, J. N. S., Idelkadi, A., et al. (2015). The impact of parametrized convection on cloud feedback. *Philosophical Transactions of the Royal Society A*, *373*(2054), 20140414.
- Zängl, G., Reinert, D., Ripodas, P., & Baldauf, M. (2014). The ICon (ICosahedral non-hydrostatic) modelling framework of dwd and MPI-m: Description of the non-hydrostatic dynamical core. *Quarterly Journal of the Royal Meteorological Society*, *141*(687), 563–579.
- Zelinka, M. D., Randall, D. A., Webb, M. J., & Klein, S. A. (2017). Clearing clouds of uncertainty. *Nature Climate Change*, *7*(10), 674.